Anomalous parity asymmetry of the CMB

Song Chen

Supervisor: *Pavel D. Naselsky*

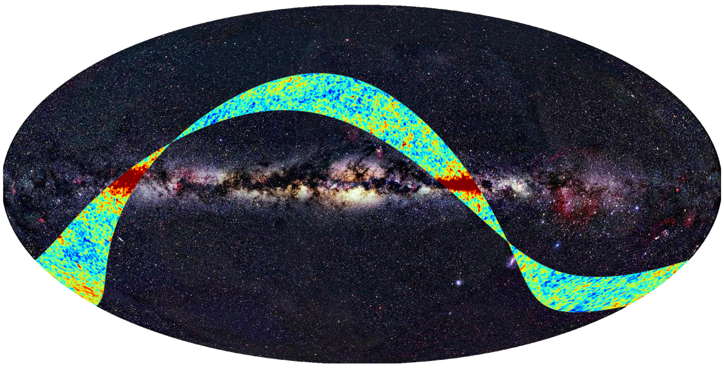

Niels Bohr Institute - Discovery Center
University of Copenhagen

A thesis submitted for the degree of
Master of Science in Physics

September 2011

Relevant Publication:

The co-author paper 'Is the CMB asymmetry due to the kinematic dipole?' is accepted by ApJ

Abstract

The symmetry test of Cosmic Microwave Background(CMB) anisotropy is one of the fundamental test of the properties of the space and time at large scale. In this thesis, I have reviewed the investigations of parity asymmetry in the CMB anisotropy, and propose a new test based on the analysis of the morphology of the CMB map through the spectral parameters of CMB fluctuations. Combined with simulations, our morphological parity test shows a significant difference of the even parity symmetry from the theoretical expectations. The results well agree that even parity map possesses an anomalous at 2-in-1000 level. The morphological analyses also imply that the theoretical even parity sky is smoother than the observed map. Since the previous investigations ruled out various non-cosmological origins, in this thesis I will focus on a possible cosmological primordial origin, i.e. the non-trivial topology model. In our investigation, the half-turn topology universe suggests that the odd parity preference could be obtained by choosing appropriate position of observer. The further discrimination between those possible origins would be given by the PLANK data. The PLANK surveyor with entirely different design and higher accuracy devices will probably greatly help us to find out the origin.

Abstract

Anisotropisymmetrien i den Kosmiske Mikrobølge baggrundsstråling er en af de fundamentale test af egenskaberne ved rum og tid påstore skalaer. I denne afhandling, har vi gennemgået tidligere undersøgelser af paritetsasymmetrien i CMB anisotropien, og vi foreslår en ny test, baseret påen analyse af morfologien af de spectrale parametre for CMB fluktuationerne påhimlen. Kombineret med simuleringer, viser vores morfologiske paritetstest, at paritetssymmetrien for lige multipoler, er markant anderledes end hvad teorien forudsiger. Resultaterne indikerer, at lige-paritetssymmetrien er unormal med en signifikans på2 ud af 1000. Morfologianalysen antyder også, at den observerede lige-paritetssymmetri har kraftigere udsving påhimlen, end forventet fra teorien. Eftersom tidligere undersøgelser har udelukket diverse ikke-kosmologiske oprindelser til paritetsasymmetrien, vil vi i denne afhandling fokusere påen mulig kosmologisk oprindelse, via en ikke-triviel topologimodel. Fra vores undersøgelser ser vi, at i et univers med 'half-turn'-topologi, kan vi forklare præferencen for ulige paritet ved at vælge en passende placering for en observatør. Yderligere præcisering af den mulige årsag kræver flere CMB-eksperimenter, og datasæt med færre bidrag fra den galaktiske forgrund og fra støj. De kommende resultater fra PLANCK satellitten, med en helt anderledes opbygning end tidligere eksperimenter, vil sansynligvis i høj grad hjælpe os til at bestemme oprindelsen til paritetsasymmetrien.

To my physics classmates...

Acknowledgements

This thesis started at October 2010 at Discovery center of Niels Bohr Institute (NBI), under the supervision of Professor Pavel D.Naselsky. I would like to thank all members of Discovery center, for their various supports. Firstly I would like to thank my supervisor, Pavel D.Naselsky, for your kindly and patiently advising. I also would like to thank Anne Mette Frejsel, Martin A.K. Hansen. You make me feel warm and happy in the group. I also appreciate Per Rex and Björn S. Nilsson, for your help in my laptop issues. I would like to thank Troels C. Petersen. Thank you for your instructions in statistics. Jaiseung Kim and Wen Zhao, thank you for your patience and useful discussion. Muo Tian, Juan Hong, Huahu Ying, my best friends, thank you for your great help for grammar checking. Last but not least, I want to thank my parents for the everything they did for me.

Contents

List of Figures

List of Tables

Chapter 1

Introduction

The Cosmic Microwave Background Radiation (CMB), was first observed by A. Penzias and R. Wilson in 1965.[1] It fills the entire universe, and it can be detected in every direction with nearly the same intensity. The observed intensity distribution show the CMB is a black body spectrum at absolute temperature of 2.725 K[2]. This black body spectrum was formed by the early hot dense plasma of photons, electrons, protons and antiparticles. Further observations discovered a small temperature fluctuation among the radiation from different angles with an average of 10^{-4} K. This temperature fluctuation is called the CMB temperature angular anisotropy.

In order to understand the origin of the CMB, and the CMB anisotropy, we need to briefly review the history of the universe. According to the standard cosmology, the Big Bang took place at approximately 13.7 billion years ago. From 10^{-36} to 10^{-32} seconds after the Big Bang, the universe underwent an extremely rapid exponential expansion, called inflation, which was the primary reason for the flat, homogeneous and isotropic universe. [3] After the inflationary period, the universe reverted to a power law expansion rate, and the temperature continued to drop. When the temperature had dropped to around 3000 K, protons and electrons were able to form stable hydrogen atoms. Before that all matter was in a plasma state and the photon mean free path was short due to Compton scattering from the charged particles and ions. After the formation of atoms, the universe are transparent. The light released at this time is perceived today (after red-shifting by the universe's expansion) as the CMB, the afterglow of the Big Bang's heat.

The CMB anisotropy actually originate from the quantum fluctuations, which can be considered as the uncertainty principle applied on the zero-point energy.[1] This zero-point energy fluctuation is basically large number of harmonic oscillators in the ground state with independent modes. Therefore, due to the central limit theorem the quantum fluctuation amplitude distribution nearly approximate to a Gaussian.[4] As a result of changing the zero-point energy, the energy density at different places will have a slight difference, resulting in the primordial density fluctuation, which is responsible for the CMB temperature anisotropy through gravitational redshift.

Accordingly, the primordial density fluctuation is statistically homogeneous and isotropic Gaussian randomly distributed on the sky, hence the CMB anisotropy should also follow a Gaussian random distribution. However, this statement has been questioned, as further investigation show that some anomalies, such as the anomalous alignments among quadrupole and octopole, the low quadrupole problem and odd-parity preference, exists in the CMB anisotropy map.

1.1 Parity symmetry

Symmetry, which can be explained as a property invariant under some transformation, is the underlying origin of all the conservation laws. The importance of the relationship between the conservation law and the symmetry was clearly recognized at the beginning of the twentieth century when the advent of special and General Relativity and the Quantum Mechanics were remarkably developed.[5]

Parity symmetry is one of the most common symmetries which corresponds to parity conservation, and can be presented as a physical quantity invariant or sign change under the following transformation:

$$P : \begin{pmatrix} x \\ y \\ z \end{pmatrix} \mapsto \begin{pmatrix} -x \\ -y \\ -z \end{pmatrix}$$

---

[1] Usually we only consider the energy difference, but the GR shows that energy itself also has important meaning, namely the spacetime curvature.

In 1956, Chen Ning Yang and Tsung-Dao (T.D.) Lee found parity conservation violation in the weak interaction [6]. Since then the parity symmetry has become more attractive, and have been tested in many other physical fields, even in the CMB [7].

Applying the parity transformation to the CMB temperature anisotropy, we find an odd parity preference. This odd parity preference can be explained by the value of the temperature deviation along a certain direction approximates to the negative value along the opposite direction for a majority of the area on the temperature anisotropy map. In the statistical perspective, there is a negative correlation between the values of the temperature deviation along two opposite directions. However, it is more natural to assume a parity-neutral universe than an odd parity universe. This anomaly was first noted by Land et al [8], but they claimed its statistical significance was not high enough. Later, Naselsky et al [9] applied a different estimator and found significant odd parity preference.

1.2 CMB surveyors

Since Penzias and Wilson first detected the CMB, various types of measurements have been carried out, including ground based telescopes, balloon borne measurements and lately, but most importantly satellites (Fig.1.1). The ground based observations and Balloon missions are all limited by earth, as they can only measure small parts of the sky. Since satellites are able to give full sky maps and ignore the absorption of CMB by the atmosphere, the CMB satellites have obtained great successes over the past years. The first CMB space mission was performed by the Cosmic Background Explorer (COBE) satellite[10], serving from 1989 to 1993, in a earth bound orbit. COBE's most important contribution is the first detection of the temperature anisotropies of the CMB. The second generation mission is the Wilkinson Microwave Anisotropy Probe(WMAP)[11]. Instead of orbiting the earth, WMAP maintains a stationary orbit with respect to sun and earth, the so called Lagrange 2 orbit. The data from WMAP is the best full-sky data before the Planck mission and plays a crucial role in establishing the current Standard Model of Cosmology. Planck, launched in 2009, is the most advanced CMB surveyor right now. Its objective is to extract all of the essential information from the CMB temperature anisotropies.[12]. Its data will expected to be released in 2012.

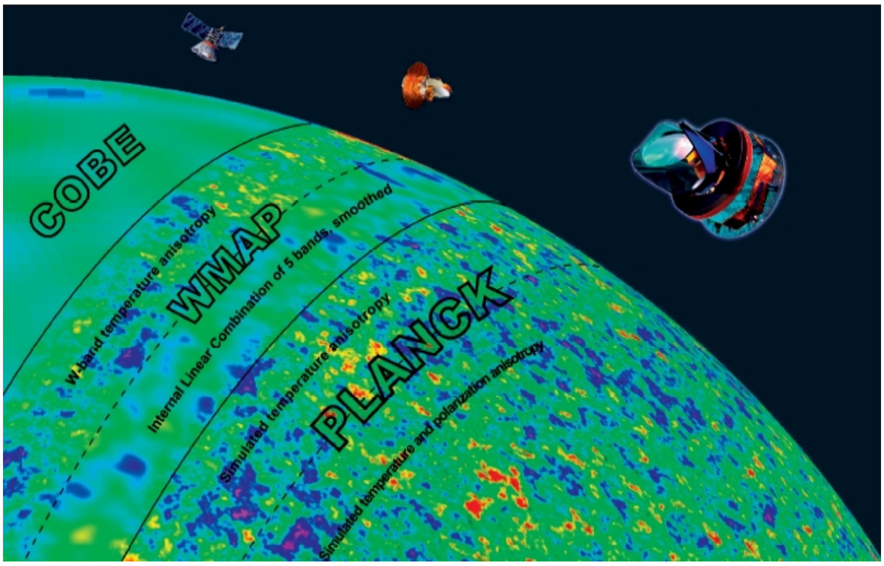

Figure 1.1: CMB surveyors - The figure shows the resolution comparison for different generation of CMB satellites. The map from Planck shows significant improvement, compared to WMAP. From the left to the right are, COBE data at a resolution of 7 degrees, WMAP 94 GHz with a resolution of about 15 arcminutes, WMAP ILC with 1 degree smoothing, simulated Planck temperature data with a resolution of around 5 arcminutes and simulated Planck polarization data smoothed to 15 arcminutes. Reprint from AAS 2006 PlanckPoster.

This thesis is organized as follows. In Chapter 2, the anomalous odd-parity preference is introduced and the previous parity test is reviewed. Chapter 3 briefly describes the morphology analyses and their parameters. Based on these morphology analyses, Chapter 4 will develop the parity spectral parameter test, and apply it to the WMAP data and simulations. In the following chapter, a possible primordial cosmological origin for the parity anomaly will be discussed. Chapter 6 concludes.

Chapter 2

Parity test review

2.1 General definitions

The temperature[1] field of the CMB, on the sphere of the entire sky can be expanded as a series of spherical harmonic oscillators

$$\Delta T(\theta,\phi) \;=\; \sum_{l=1}^{\infty}\sum_{m=-l}^{l} a_{lm}Y_{l,m}(\theta,\phi)\,. \tag{2.1}$$

The temperature difference ΔT, is a sum of spherical harmonics multiplied by a coefficient of decomposition a_{lm}. Under the hypothesis of homogeneity and isotropy, the power spectrum ${C_l}$[2] can be defined as

$$< a_{lm}a_{l'm'} >= \delta_{l,l'}\delta_{m,m'}C_l\,. \tag{2.2}$$

Its Fourier pair, i.e. the two-point correlation function, can be written as

$$< \Delta T\ (\hat{q_1})\ \Delta T\ (\hat{q_2})) > =\ C(\theta) = \frac{1}{4\pi}\sum_{l}^{\infty}(2l+1)C_l W_l P_l(\cos\theta)\,, \tag{2.3}$$

where θ is the relative angle between $\hat{q_1}$ and $\hat{q_2}$, and P_l is Legendre polynomial. W_l is the window function of the observation, which converts the observed 'temperature' to the ideal temperature[3]. According to Silk & Wilson (1980) and Bond & Efstathiou

---

[1] The 'temperature' we discussed in this thesis is the CMB temperature anisotropy

[2] What we calculate C_l from the map actually is a estimator of this.

[3] In fact, they assign a 'temperature' or 'temperature difference', since no real experiment can measure the ideal temperatures. For more about Window function see M.White and M.Srednicki 1994 [13]

(1984), the window function for a Gaussian beam can be written as

$$W_l \approx e^{-\frac{1}{2}l(l+1)\sigma^2}, \tag{2.4}$$

where σ is the standard deviation of the Gaussian beam, which related to the resolution as $\theta_{FWHM} = \sqrt{8\ln 2}\sigma$. The window function falls off sharply at large l, namely $l \sim \sigma^{-1}$. The relation between $C(\theta)$ and θ is characterized by Fig.2.1. We may see from Fig.2.1 that there is a non-negligible discrepancy between the observed data and the theoretical prediction. Kim and Naselsky found that this discrepancy, in fact, originate from odd-parity preference at low multipoles.

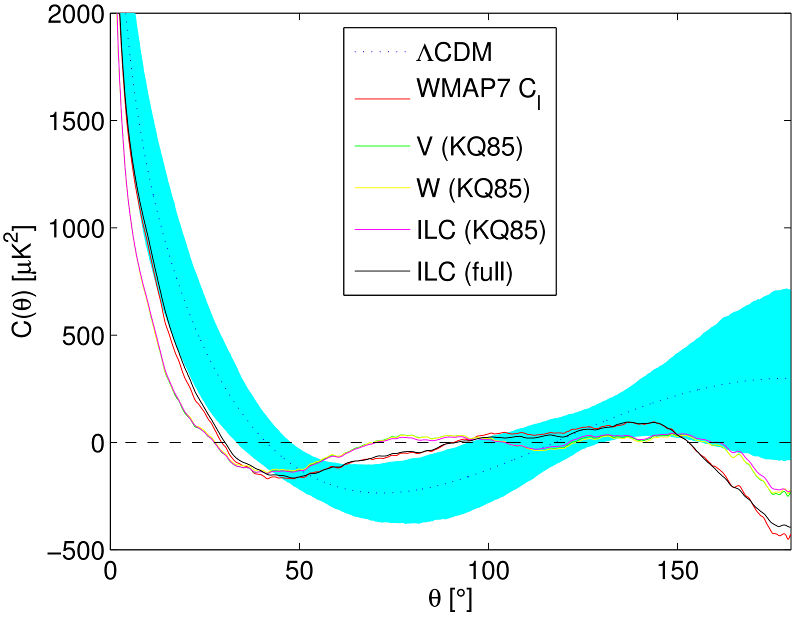

Figure 2.1: The two point angular correlation - Blue region denotes the standard deviation σ of Monte Carlo simulations. The figure shows the deviation between ΛCDM model and WMAP ILC 7 years data. This figure is from Kim and Naselsky[14]

2.2 Parity preference of CMB

In order to discuss parity symmetry, a few estimators and concepts are need to be introduced.

Firstly, let us consider CMB temperature field as a linear combination of the even and odd parity temperature fields, i.e.,

$$T(\hat{n}) = T^{+}(\hat{n}) + T^{-}(\hat{n})\,, \tag{2.5}$$

where[1]

$$T^{+}(\hat{n}) = \frac{T(\hat{n}) + T(-\hat{n})}{2}\,, \tag{2.6}$$

$$T^{-}(\hat{n}) = \frac{T(\hat{n}) - T(-\hat{n})}{2}\,. \tag{2.7}$$

As a result of the parity property of spherical harmonics, the temperature field can be described as a linear combination of even or odd spherical harmonics,

$$Y_{lm}(-\hat{n}) = (-1)^{l} Y_{lm}(\hat{n}) \tag{2.8}$$

$$T^{+}(\hat{n}) = \sum_{l,m} \Gamma^{+}(l) a_{lm} Y_{lm}(\hat{n}) \tag{2.9}$$

$$T^{-}(\hat{n}) = \sum_{l,m} \Gamma^{-}(l) a_{lm} Y_{lm}(\hat{n}) \tag{2.10}$$

where $\Gamma^{+}(l) \equiv \cos^{2}(\frac{\pi l}{2})$ and $\Gamma^{-}(l) \equiv \sin^{2}(\frac{\pi l}{2})$.

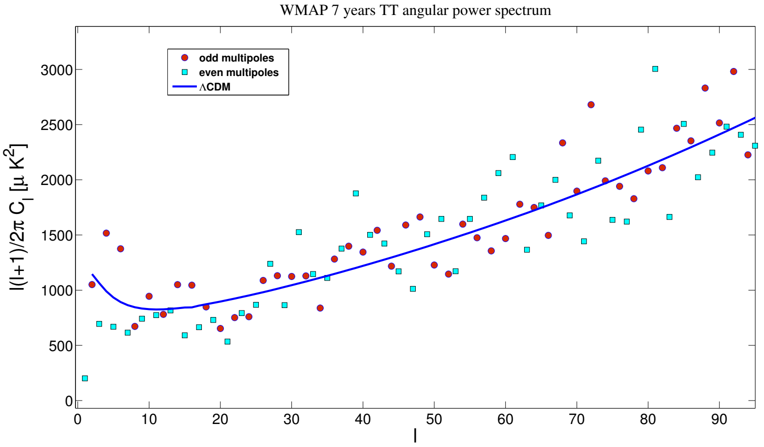

Figure 2.2: WMAP 7 years angular power spectrum - Power spectrum at even multipoles tend to be lower than those at neighboring odd multipoles.

---

[1] The CMB temperature anisotropy map uses Galactic coordinate, which is centered on the Sun. In other words, the origin of $\hat{n}$ is the Sun.

In Fig. 2.2, we can conclude that, in the range of 2 to 22, even multipoles tend to be lower than the odd multipoles. All the even multipoles in the range of 2 to 22 are below the ΛCDM prediction.

By defining a quantity P^+/P^-, we could measure the parity preference, where P^+ and P^- are the sum of the even and odd multipoles respectively[14].

$$P^+ = \sum_{l=2}^{l_{max}} \frac{1}{4\pi}\Gamma^+(l)l(l+1)C_l \tag{2.11}$$

$$P^- = \sum_{l=2}^{l_{max}} \frac{1}{4\pi}\Gamma^-(l)l(l+1)C_l \tag{2.12}$$

Hence, the ratio P^+/P^- indicates the degree of the parity asymmetry. As shown in Fig. 2.3, the theoretical ΛCDM model looks like a mirror image of WMAP data with respect to the line $P^+/P^- = 1$.

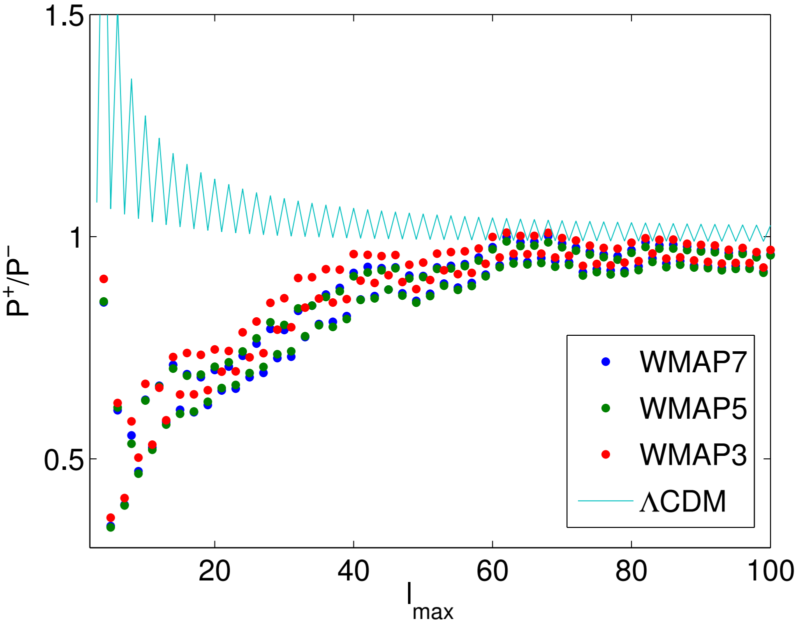

Figure 2.3: Parity asymmetry test for WMAP 3,5,7 years - The blue line show the P^+/P^- of ΛCDM model and colorful points show P^+/P^- of WMAP.(Kim and Naselsky 2010)

Through simulation, we can describe how odd this ratio is. Firstly, we define the probability p-value as the fractions of simulations that are below the WMAP P^+/P^- value, which depends on the upper limit of the sum(l_{max}). Hence, we can draw a plot of the p-value with respect to different l_{max}, as shown in Fig.2.4. The minimum of the curve, obtained from Fig.2.4, is around $l_{max} = 22$, and its p-value is 0.31% for WMAP 7 years compared to 10,000 simulations (Kim & Naselsky 2010[14]). Gruppuso et al.(2010)[15] confirmed this parity anomaly in a different way. This fact indicates that we may not simply attribute this parity asymmetry to the low quadrupole anomaly.

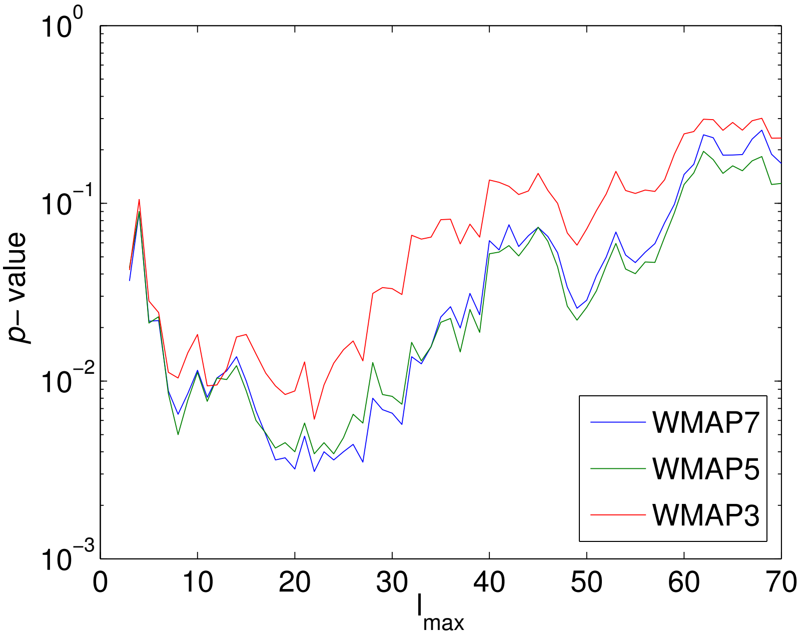

Figure 2.4: p-value for different l_{max} - Kim and Naselsky 2010

Moreover Naselsky and Kim [16] discussed the Marginalized likelihood of cosmological parameters, since the power spectrum is mainly used to fit cosmological models. As shown in Fig.2.5, the anomaly in the power spectrum create a non-negligible tension in the parameters of the primordial power spectrum. In other words, the even and odd multipoles theoretically should originate from the same fluctuation, but the observation indicates they correspond to two totally different cosmological models. As a result, if we eventually find out the origin of odd parity preference is a systematic error, then the standard cosmological model will be changed.

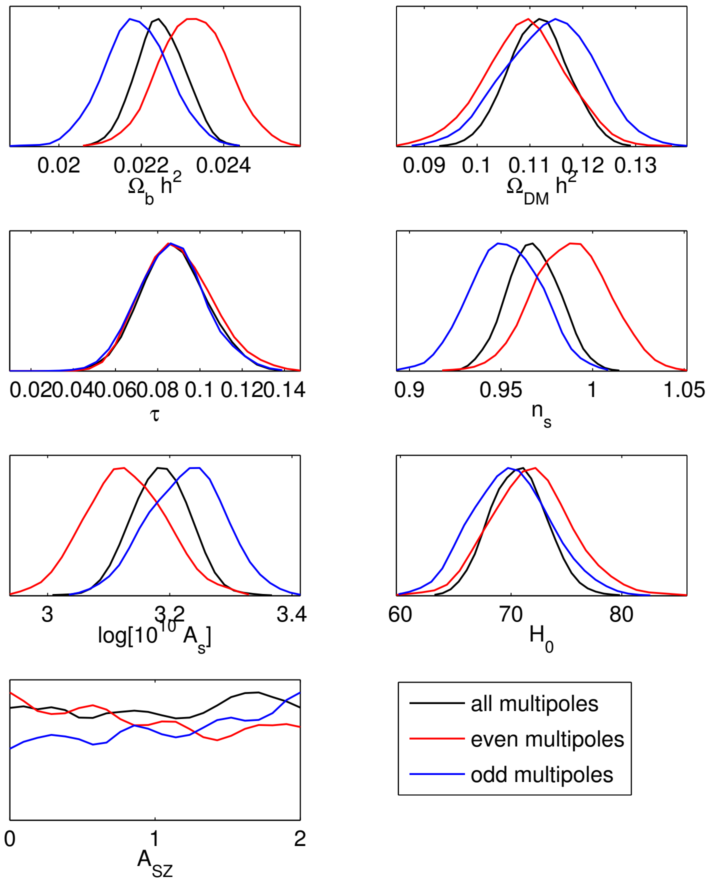

Figure 2.5: Marginalized likelihood of cosmological parameters - results are obtained respectively with even or odd multipole data.

Chapter 3

Morphology test

In order to find out the origin of this anomaly, firstly we need to know which parity is 'wrong', even or odd. The comparison of power spectra is unable to identify the peculiar parity symmetry, since both even and odd multipoles oscillate around the theoretical value with roughly the same amplitude. Similarly, it is also impossible to identify it from the cosmological parameters (Fig.2.5). Therefore, we change our focus from the power spectrum to the temperature anisotropy map. The morphology analysis which is one of the best way to explore the map's geometrical and topological properties, will be used in the following investigation.

3.1 One-point probability density distribution function

The most intuitive method to analyze the temperature anisotropy map, is to make a histogram of pixels all over the map, then compare this histogram to the ΛCDM model. This method is named one-point probability density distribution function(p.d.f) test. The theoretical p.d.f is the standard Gaussian probability density function with zero mean[1]. The standard deviation σ of the theoretical p.d.f can be calculated from the angular correlation function $C(\theta)$ by setting θ to 0.

---

[1] If we ignore the effect of the correlated neighbor pixels

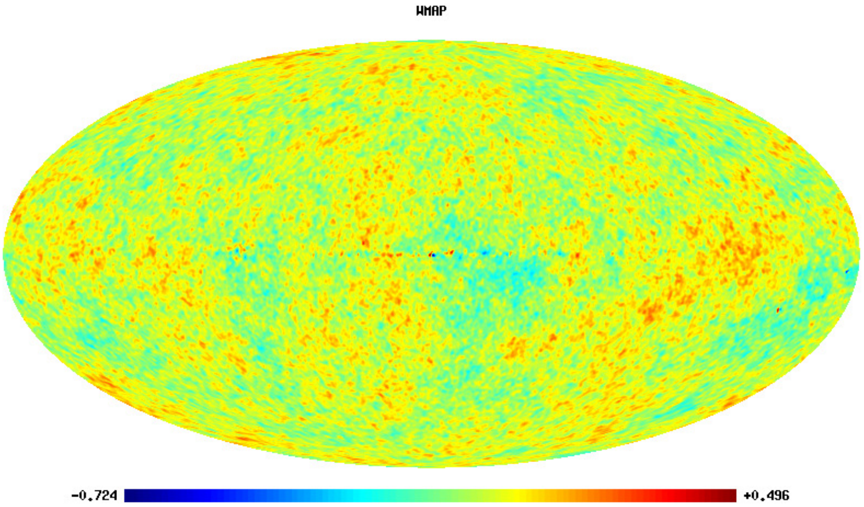

Figure 3.1: CMB Temperature Anisotropy Map - WMAP 7 years ILC map

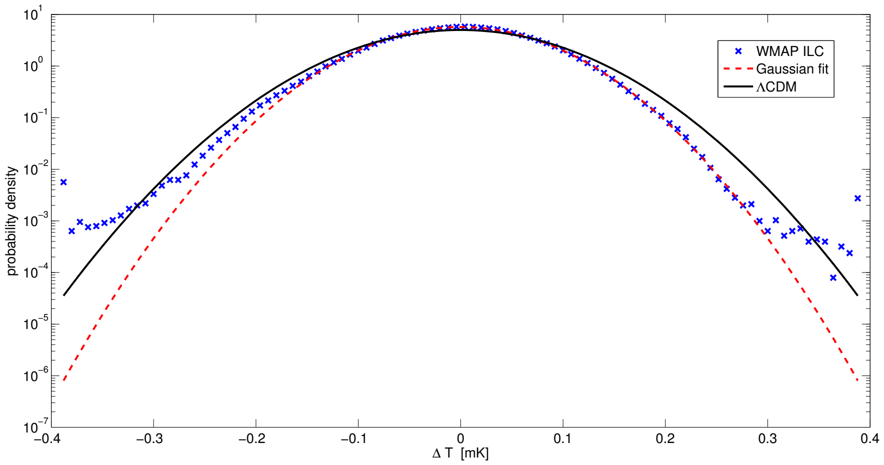

Figure 3.2: One-point p.d.f - One-point p.d.f of WMAP 7 years ILC map (Fig.3.1)

It is worthwhile to emphasis, that the map we used here is WMAP 7 years Internal Linear Combination (ILC) map, which is a foreground cleaned map, formed from a weighted linear combination of the 5 smoothed maps. The weights are chosen to minimize the Galactic foreground contamination. However, ILC map is definitely not an ideal map. Figure 3.2 illustrates the deviation between the WMAP 7 years ILC map and the ΛCDM model, where the theoretical p.d.f is calculated by using the ΛCDM model best-fit power spectrum associated with a 1 degree resolution window function.

The test result indicates that the deviation between the observed data and the ΛCDM model predication is non-negligible. On the other hand, basically the p.d.f of the observed data, is following a Gaussian p.d.f, therefore it is reasonable to utilize the morphology analysis of a Gaussian random field. Furthermore, When compare to the best fit curve, the deviation is mainly located at values smaller than -0.15. By drawing the WMAP ILC map for specified temperature ranges, we find some isolated pixels, some of them are probably the non-Gaussian noise[1], see Fig.3.3.

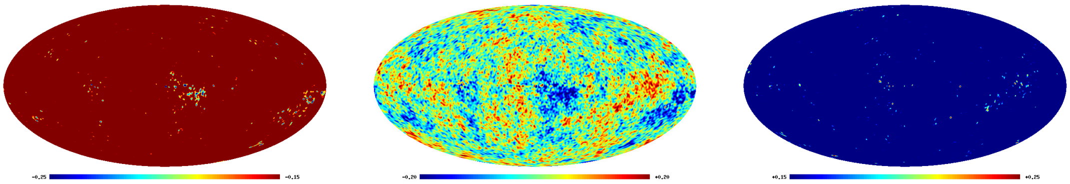

(a) -0.25 to -0.15 (b) -0.2 to 0.2 (c) 0.15 to 0.25

Figure 3.3: ILC map for different temperature range

3.2 Minkowski functionals

The Minkowski functionals, the most famous morphological analysis, can be quantified as a set of measurements concerning the geometrical and topological properties of a random field (Minkowski 1903). It belongs to the branch of mathematics so called integral geometry, introduced into cosmology by Mecke, Buchert and Wagner (1994)[17]. Minkowski functionals describe the properties of the field, which are invariant under transformations like translation, rotation or their linear combination. It can be employed for both the full sky and an incomplete coverage of the sky. For more details see D.Novikov (1999)[18].

In 1957 Hadwiger [19] showed that all global morphological properties of any D-dimensional space can be completely described using D+1 Minkowski functionals. In our case, the two dimensional map can be completely described by three Minkowski functionals, which are, the area of the map above a certain temperature threshold

---

[1] The deviation could also be attributed to the effect of the correlated neighbor pixels.

(A), its boundary length (L), and its Euler-Poincaré characteristic (G)(or equivalently, its topological genus, or number of holes). For the 2D Gaussian random field, the Minkowski functionals are known as

$$A(\nu) = \frac{1}{2} - \frac{1}{2}\phi(\frac{\nu}{\sqrt{2}})\,, \tag{3.1}$$

$$L(\nu) = \frac{1}{8\theta_c}\exp(-\frac{\nu^2}{2})\,, \tag{3.2}$$

$$G(\nu) = \frac{1}{(2\pi)^{\frac{3}{2}}}\frac{1}{\theta_c^2}\nu\exp(-\frac{\nu^2}{2})\,. \tag{3.3}$$

where $\nu = \frac{\Delta T}{\sigma_0}$, σ_0 is the standard deviation of the field. Since the Minkowski functionals for a Gaussian random field are analytical, these functionals become a common tool for testing non-Gaussianity.

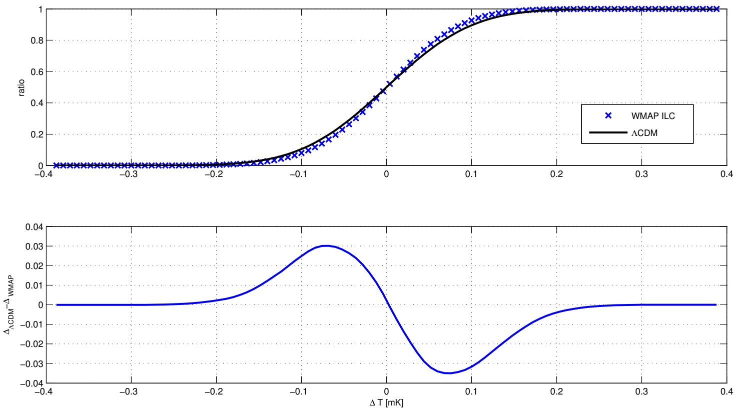

Figure 3.4: The 1st Minkowski function - The upper figure is the One-point cumulative distribution function and the lower figure is the difference between theory and observation.

In the previous section, we have used a one-point p.d.f test for the temperature anisotropy map. Actually, the one-point cumulative distribution function and the first Minkowski functional $A(\nu)$ are equivalent, because the number of pixel in the map is equivalent to the area of the map. According to the definitions, the accumulative function of the pixels histogram exactly describes the area of the map which is above a certain temperature threshold.

The test result of the first Minkowski functional(WMAP 7 years ILC) is shown in Fig.3.4. $A(\nu)$ as shown in Eq.3.1, is the only function that is independent of any parameters. From Eq. 3.1 we note that the last two functions possess a parameter, namely the length scale of the field θ_c.

$$\theta_c = \frac{\sigma_0}{\sigma_1}\,, \tag{3.4}$$

where σ_1^2 is the variance of the first derivative of the field. Mathematician call it mean square derivative. σ_0 and σ_1 can be calculated using the spectrum Cl,

$$\begin{aligned}
\sigma_0^2 &= \frac{1}{4\pi}\sum_l (2l+1)C_l W_l\,, && (3.5)\\
\sigma_1^2 &= \frac{1}{4\pi}\sum_l (2l+1)(l+1)lC_l W_l\,, && (3.6)\\
\sigma_2^2 &= \frac{1}{4\pi}\sum_l (2l+1)[(l+1)l(l-1)(l+2)+\frac{4(l+1)l}{3}]C_l W_l\,. && (3.7)
\end{aligned}$$

In addition, σ_i are actually called spectral parameters. They are the key parameters, which dominate the morphological properties of Gaussian random field(see Chapter 4). Accordingly our investigation will focus on the spectral parameters, and the rest Minkowski functional tests will not be repeated in this thesis.

3.3 Cluster analysis

Similar to Minkowski functionals, cluster analysis is also a topological method for the sky maps analysis. This method is based on the assumption that the background radiation forms a two-dimensional Gaussian random field.

The statistical properties of a Gaussian random field were first investigated by Rice (1944,1945) for a one-dimensional field, to analyze electrical noise in communication devices. A. Doroshkevich (1970) was the first who applied this theory extensively in the study of the cosmic structure formation. J.Bardeen J.Bond, N.Kaiser and A.Szalay (1986)(referred to as BBKS) developed the theory for a three-dimensional field in their classic paper, and the two-dimensional field version was developed by J.Bond & G.Efstathiou (1987)(referred to as BE). Finally, Novikov and Jørgensen (1996)[20] completed the theory of peak clusterization in a random Gaussian field, by adding analytical calculations for saddle points.

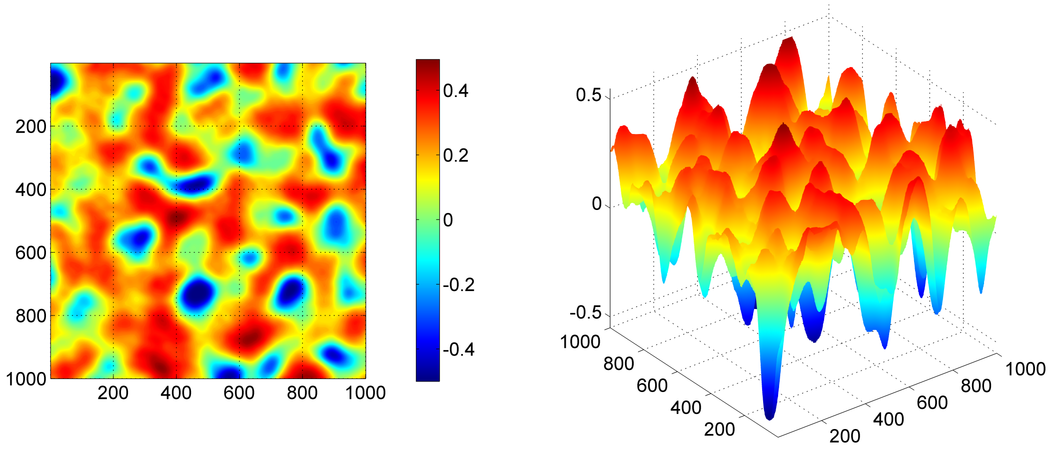

Figure 3.5: Schematic diagram for ΔT surface - The temperature anisotropy peaks is shown above.

When we look at a picture of the temperature anisotropy, we see the color distributing itself randomly on the map from warm to cold. The cold and warm colors correspond to the lower and higher temperature, which indicate that the wavelength of the light is longer and shorter. This wavelength difference is due to the gravitational redshift. As displayed in Fig.3.5, a two-dimensional temperature field can be described as a curved surface living in three-dimensional space. The surface is called hypersurface, which can be divided into several contours. The cluster of peaks are defined as a collection of maxima confined by a specified single contour, see Fig. 3.6. The number of peaks in a cluster is called the cluster length. It highly depends on the contour level factor, defined as

$$\nu_t = \frac{\Delta T}{\sigma_0} . \tag{3.8}$$

The contour is also a random function, because it comes from a section of the temperature field ΔT, which is assumed to be a two-dimensional Gaussian random field.

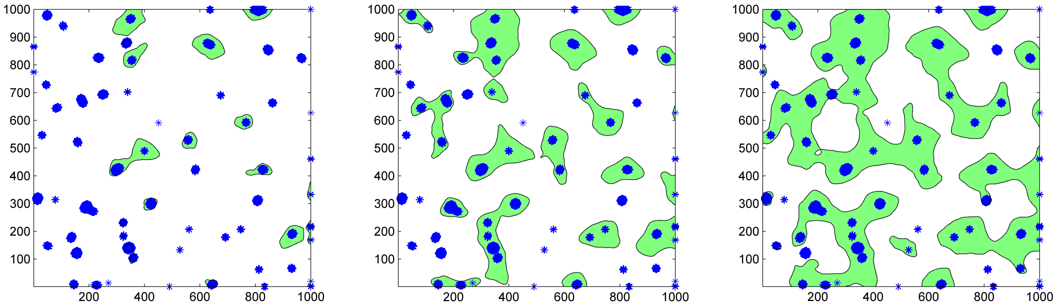

Figure 3.6: Length of clusters for different levels - The level of contours decrease from left to right. The mean length of clusters of maxima increases, and the blue asterisks correspond to local maxima peaks.

More specifically, let us take a look at the mathematical description of the cluster of peaks. The density of maxima and minima for the two dimensional Gaussian field was derived by BE as

$$N_{max}(\nu)\mathrm{d}\nu = \frac{1}{2\pi R_*^2} exp(-\nu^2/2)\frac{\mathrm{d}\nu}{(2\pi)^{\frac{1}{2}}} G(\gamma, \gamma\nu)\,, \tag{3.9}$$

$$\begin{aligned} G(\gamma,\chi_*) \quad &\equiv \quad (\chi_*^2-\gamma^2)[1-\frac{1}{2}\mathrm{erfc}(\frac{\chi_*}{[2(1-\gamma^2)]^{\frac{1}{2}}})] + \chi_*(1-\gamma^2)\frac{\exp(-\chi_*/[2(1-\gamma^2)])}{[2\pi(1-\gamma^2)]^{\frac{1}{2}}}\,, \\ &+ \quad \frac{\exp(-\chi_*^2/(3-2\gamma^2))}{(3-2\gamma^2)^{\frac{1}{2}}}[1-\frac{1}{2}\mathrm{erfc}(\frac{\chi_*}{[2(1-\gamma^2)(3-2\gamma^2)]^{\frac{1}{2}}})] \end{aligned} \tag{3.10}$$

where $\gamma = \frac{\sigma_1^2}{\sigma_0\sigma_2}$ and $R_* = \sqrt{2}\sigma_1/\sigma_2$. When $\nu \to \infty$, $G \to \gamma^2(\nu^2-1)$.

$$N_{min}(\nu) = N_{max}(-\nu) \tag{3.11}$$

The differential density of the saddle points is

$$N_{sad}(\nu)\mathrm{d}\nu = \frac{1}{\sqrt{8\pi^3}}\frac{1}{R_*^2\sqrt{3-2\gamma^2}}\exp(\frac{-3\nu^2}{2(3-2\gamma^2)})\mathrm{d}\nu \tag{3.12}$$

The differential density distribution of maxima, minima and saddle points are very sensitive to γ , see Fig.3.7. The number of maxima,minima and saddle points above a certain threshold ν_t is the integration of the above equations 3.9-3.12 from ν_t to infinity.

$$\begin{aligned} n_{max}(\nu_t,\gamma) &= \int_{\nu_t}^{\infty} N_{max}\mathrm{d}\nu \\ n_{saddle}(\nu_t,\gamma) &= \int_{\nu_t}^{\infty} N_{saddle}\mathrm{d}\nu \\ n_{min}(\nu_t,\gamma) &= \int_{-\infty}^{\nu_t} N_{min}\mathrm{d}\nu \end{aligned} \tag{3.13}$$

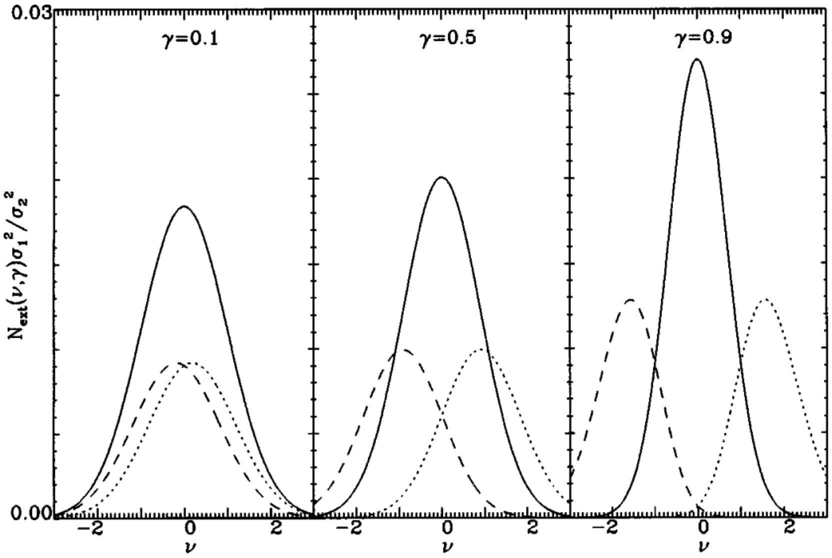

Figure 3.7: Differential density distribution - Differential density distribution of maximum(*dotted line*), saddle points(*solid line*) and minimum(*dashed line*).This figure is from D.I.Novikov and H.E.Jørgensen (1996)

In order to show that the rate of clustering depends on γ, the mean cluster length k at level ν_t needs to be introduced.

$$\langle k\rangle = \frac{\sum_k kN_k}{\sum_k N_k} \tag{3.14}$$

The numerator is the summation of maximum in all clusters, which equals the total number of maxima.

$$\sum_{k=1}^{\infty} kN_k \ = \ n_{max}(\nu_t) \tag{3.15}$$

The denominator is the sum of the number of clusters.

$$\sum_k N_k = n_{max}(\nu_t) + n_{min}(\nu_t) - n_{sad}(\nu_t) \tag{3.16}$$

Hence, in one cluster the number of saddle and number of maxima and minima are not independent.

$$k_{saddle} = k_{max} + k_{min} - 1 \tag{3.17}$$

Thus,

$$\sum_{cluster} 1 = \sum k_{max} + \sum k_{min} - \sum k_{saddle} \tag{3.18}$$

So far, we have derived the mean cluster length as:

$$\langle k\rangle(\nu_t,\gamma) = \frac{n_{max}(\nu_t,\gamma)}{n_{max}(\nu_t,\gamma) + n_{min}(\nu_t,\gamma) - n_{saddle}(\nu_t,\gamma)} \tag{3.19}$$

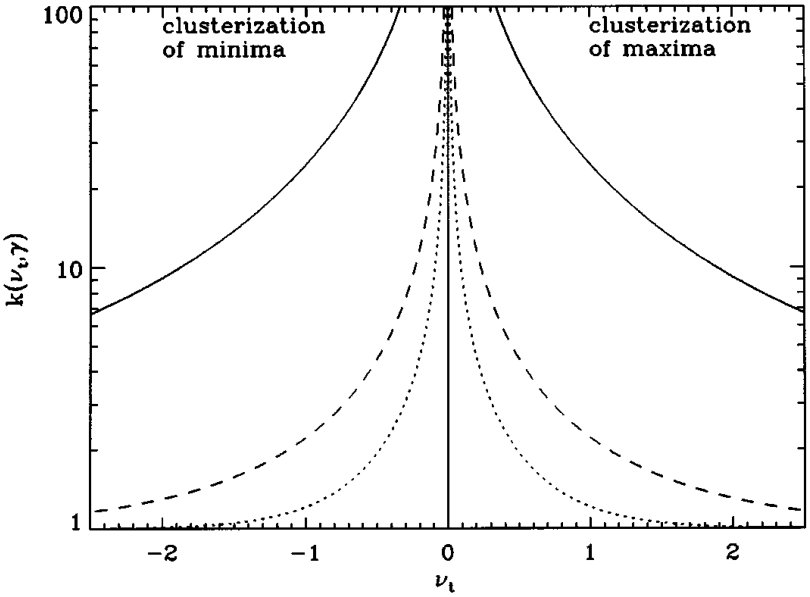

Figure 3.8: Mean length of clusters for different γ - *Solid line* for $\gamma = 0.1$,*dashed line* for $\gamma = 0.5$,*dotted line* for $\gamma = 0.9$. When the level of contour is sufficient high, almost all the extrema are maxima $n_{min} \approx 0$ and $n_{sad} \approx 0$ thus, $\langle k\rangle \approx 1$. If $\nu_t \approx 0$, $n_{max}+n_{min}-n_{sad}$ tends to zero, hence $\langle k\rangle \approx \infty$. This figure is from D.I.Novikov and H.E.Jørgensen (1996)

After plugging Eq.3.13, Eq.3.9 and Eq.3.12 in, it is clear that the function of mean cluster length at level ν_t has only one parameter γ. As illustrated in Fig.3.8, γ is inversely proportional to the clustering speed[1]. Therefore, it is hard to overemphasize that the spectral parameter γ dominates the clustering of the peaks which is one of the most important topological properties in a 2 dimensional Gaussian random field. Accordingly, γ will be one of the important aspects in the following discussion. Besides, cluster analysis can also be used to test point like sources, because the noise will strongly shift the mean cluster length at some contour level. Since all the analytical results above are based on the Gaussian random field assumption, the result for any other field will

---

[1] Note γ lies between 0 and 1.

probably differ a lot. From this point of view, the distribution of clusterization could be used to test non-Gaussianity as well.

Chapter 4

Morphology analysis

In this chapter the morphology analysis method will be employed to the parity symmetry test, and three new parity tests, which associated with the geometrical and topological properties, will be introduced. Finally the most peculiar parity will be revealed and discussed.

4.1 Morphology in terms of spectral parameters

The objective of the morphology analysis is to investigate the geometrical and topological properties of a random field. More specifically, this method studies the temperature radiation pattern. Theoretically, all the results from the analysis is dependent on the statistical quantities of the random field, namely the mean of the field, variance of field and variance of the field's nth order derivative and etc. For instance, in the previous chapter, both the Minkowski functionals and the cluster analysis are associated with these statistical quantities, which are called spectral parameters.

According to BBKS(The statistics of peaks of Gaussian random fields 1986[21]), the variance of the field's jth order derivative in 3 dimensions is defined as:

$$\sigma_j^2 \equiv \int \frac{k^2 \mathrm{d}k}{2\pi^2} P(k) k^{2j} \tag{4.1}$$

where k is the Fourier transform pair of the spacial coordinate r, and $P(k)$ is the power spectrum. Apparently, it is complicated to calculate the integration, but mathematicians found a possible way to resolve it, by changing the integration into partial derivatives. According to Adler (1981)[22],

$$\sigma_j^2 \equiv \int \frac{k^2 \mathrm{d}k}{2\pi^2} P(k) k^{2j} = (-1)^j \frac{\partial^2 C(r)}{\partial r^2} |_{r=0} \tag{4.2}$$

The $2j$th-order spectral moments are equal to the appropriate $2j$th partial derivative of correlation function at the origin times a coefficient $(-1)^j$. In this equation, the correlation function $C(r)$ and the power spectrum $P(k)$ form a Fourier transform pair (Wiener-Khinchin theorem).

$$P(k) = \int C(r) e^{i\vec{k}\cdot\vec{r}} dr^2 \tag{4.3}$$

$$C(r) = \int P(k) e^{-i\vec{k}\cdot\vec{r}} dk^2 \tag{4.4}$$

As a result of isotropy, the power spectrum only depends on the magnitude of k. Thus, the angular part of the integration $\int_0^{2\pi} d\phi \ e^{i|k|\cdot|r|\, cos(\phi)}$ can be carried out, which is proportional to $J_0(kr)$, i.e. the order zero Bessel function. Thus, Eq.4.3 and Eq.4.4 can be rewritten as:

$$P(k) = \int C(r) J_0(kr) r dr \tag{4.5}$$

$$C(r) = \int P(k) J_0(kr) k dk \tag{4.6}$$

This two dimensional Fourier transform of a circularly symmetric function is called a zero-order Hankel transform. $C(r)$ and $P(k)$ are unfamiliar to us, but $C(\theta)$ and C_l are well-known. $C(r)$ and $P(k)$ are defined in a 3 dimensional flat space, while $C(\theta)$ and C_l are defined on a 2 dimensional sphere. In order to express $C(r)$ and $P(k)$ in terms of $C(\theta)$ and C_l, we employ the so-called 'flat-sky' approximation, which denotes that a small area of the sphere is considered to be flat. By employing appropriate projection method, we can study the statistical properties of the temperature map in the flat plane.

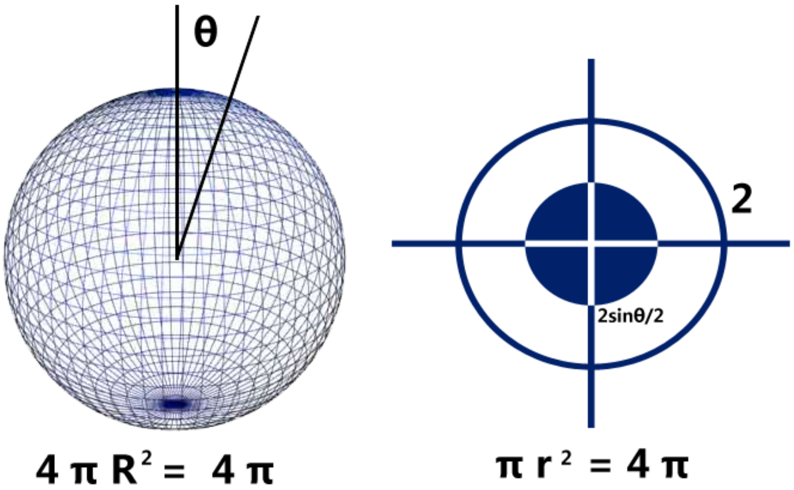

Figure 4.1: Equal area projection - This method project the sphere on to a plane with equal area. $4\pi = \pi r^2 = \pi(2sin(\frac{\pi}{2}))^2$

Here, we use the projection method given by J.R.Bond and G.Efstathiou's (1987)[23]. We may consider the coordinate with an arbitrary chosen 'North Pole' of the sky, and choose polar coordinates (r , ϕ), where ϕ is longitude, and

$$r = 2sin(\frac{\theta}{2}) \tag{4.7}$$

where θ is colatitude, see Fig. 4.1.[1] [2]

Now, considering the two point correlation $C(r)$, If we set one point at the center of the disk(North Pole in the sphere), then r describes the distance between a arbitrary point and center of disk, i.e. radius.[3] Recall in Eq.4.2, the variance of the field's nth derivative only related to the partial derivative of $C(r)$ at $r = 0$, When r is small, θ approximate to r. By coincidence $\theta = 0$ is the 'North Pole' of the sky. The distortion of the projection (from sphere to plane) is minimized in the neighborhood of the North Pole. Hence, the error in σ_i is sufficiently small.[4]

---

[1] we choose colatitude instead of latitude because when the point is close to the North Pole it is easy to see the curved sphere surface approximate to a flat plane.

[2] we choose $r = 2sin(\frac{\theta}{2})$ because we want to make an equal area mapping of a disc of radius 2 on to the sphere and $2sin(\frac{\theta}{2})$ is nothing but the radius of the disc, see Fig. 4.1.

[3] As a consequence of homogeneity and isotropy, the two points correlation function do not depend on the direction.

[4] The error still exist, especially for the full-sky investigation.

In the limit of large l and small θ,

$$P_l(cos\theta) \approx J_0[(l+\frac{1}{2})\theta] \tag{4.8}$$

therefore,

$$P(k) \approx C_l \quad k \approx l/\eta_0 \tag{4.9}$$

It is obvious that

$$\begin{aligned} C(r) &\approx C(\theta) \\ \int_0^2 P(k)J_0(kr)kdk &\approx \frac{1}{4\pi}\sum_l^\infty(2l+1)C_lP_l(Cos\theta) \end{aligned} \tag{4.10}$$

Therefore it is reasonable to use $C(\theta)$ and C_l instead of $C(r)$ and $P(k)$ in the calculation of spectral parameters.

Finally, spectral parameter σ can be written as:

$$\sigma_0^2 = C(0) \tag{4.11}$$

$$\sigma_1^2 = \frac{d^2C(r)}{dr^2} \tag{4.12}$$

$$\sigma_2^2 = \frac{d^4C(r)}{dr^4} \tag{4.13}$$

where

$$\frac{dC(r)}{dr} = \frac{dC(r)}{d\theta}\frac{d\theta}{dr} = \frac{dC(\theta)}{d\theta}|_{\theta=0} \tag{4.14}$$

The coefficient at the font of derivative, comes from partial derivative of the Bessel function $J_0(kr)$ at the origin. Instead of e^{ikr}, the Bessel function $J_0(kr)$ is not equal to one, when r approaches zero.

$$\frac{dJ_0^2(kr)}{dr^2}|_{r=0} = -\frac{k^2}{2} \tag{4.15}$$

$$\frac{dJ_0^4(kr)}{dr^4}|_{r=0} = \frac{3k^4}{8} \tag{4.16}$$

we can express those parameters in terms of the derivatives of the angular correlation function at the origin.

$$\sigma_1^2 = 2C''(0) \tag{4.17}$$

$$\sigma_2^2 = \frac{8}{3}C^{(4)}(0) \tag{4.18}$$

Two useful expressions of Legendre Polynomials for deriving the above equations is shown below:

$$P'_l(1) = \frac{l(l+1)}{2} \tag{4.19}$$

$$P''_l(1) = \frac{l(l+1)(l-1)(l+2)}{8} \tag{4.20}$$

The final formula of sigmas are shown in Eq.3.5. It is worthwhile to note that the result of σ_2^2 is different from J.R.Bond G.Efstathiou's[23] for a factor $\frac{4(l+1)l}{3}$ inside the summation. This factor has big influence when l is small as shown in Fig.4.2. In fact, BE's σ_2^2 could be considered as a good approximation when the angular scale is small.

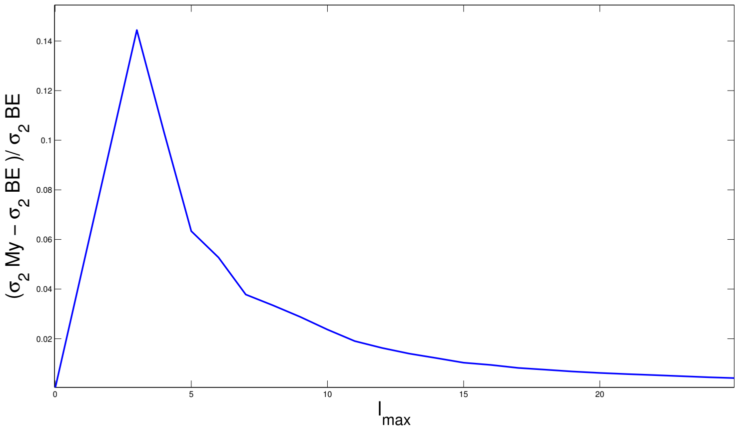

Figure 4.2: σ_2^2 parameter difference - This figure shown the difference between my formula and Bond & Efstathious,the x axle is the upper limit of sum, the y axle is my σ_2^2 minus BE's σ_2^2 divide by BE's σ_2^2. As shown in the figure, difference is only exist at small l.

Besides those variances, It is worthwhile to note three combinations of σ_i which have important meaning for some morphology analyses.

$$\theta_c \equiv \frac{\sigma_0}{\sigma_1} \tag{4.21}$$

$$R_* \equiv \frac{\sqrt{2}\sigma_1}{\sigma_2} \tag{4.22}$$

$$\gamma \equiv \frac{\sigma_1^2}{\sigma_0\sigma_2} \tag{4.23}$$

In the case of a Gaussian random field, Minkowski functions have only one parameter θ_c. The peak cluster properties are described by two parameters R_* and γ, where R_*

determines the number of local maxima per unit square, and γ is the parameter of the clustering of peaks. Consequently, the result of the spectral parameter analysis will definitely influence the results of the Gaussian field morphology analysis.

4.2 Analysis of even and odd parity maps in terms of spectral parameters

Considering the parity asymmetry, the spectral parameters are divided into an even part and an odd part. The even and odd part of those parameters are related to $T^+(\hat{n})$ and $T^-(\hat{n})$ fields. Since $T^+(\hat{n})$ and $T^-(\hat{n})$ are associated with the power spectrum of even and odd multipoles, we may define:

$$(\sigma_0^e)^2 = \frac{1}{4\pi}\sum_l \Gamma^+(l)(2l+1)C_l W_l \tag{4.24}$$

$$(\sigma_0^o)^2 = \frac{1}{4\pi}\sum_l \Gamma^-(l)(2l+1)C_l W_l \tag{4.25}$$

$$(\sigma_1^e)^2 = \frac{1}{4\pi}\sum_l \Gamma^+(l)(2l+1)(l+1)lC_l W_l \tag{4.26}$$

$$(\sigma_1^o)^2 = \frac{1}{4\pi}\sum_l \Gamma^-(l)(2l+1)(l+1)lC_l W_l \tag{4.27}$$

$$(\sigma_2^e)^2 = \frac{1}{4\pi}\sum_l \Gamma^+(l)(2l+1)[(l+1)l(l-1)(l+2)+\frac{4(l+1)l}{3}]C_l W_l \tag{4.28}$$

$$(\sigma_2^o)^2 = \frac{1}{4\pi}\sum_l \Gamma^-(l)(2l+1)[(l+1)l(l-1)(l+2)+\frac{4(l+1)l}{3}]C_l W_l \tag{4.29}$$

$$\theta_c^e = \frac{\sigma_0^e}{\sigma_1^e}; \quad R_*^e = \frac{\sqrt{2}\sigma_1^e}{\sigma_2^e}; \quad \gamma^e = \frac{(\sigma_1^e)^2}{\sigma_0^e\sigma_2^e} \tag{4.30}$$

$$\theta_c^o = \frac{\sigma_0^o}{\sigma_1^o}; \quad R_*^o = \frac{\sqrt{2}\sigma_1^o}{\sigma_2^o}; \quad \gamma^o = \frac{(\sigma_1^o)^2}{\sigma_0^o\sigma_2^o} \tag{4.31}$$

where $\Gamma^\pm$ following the definition in Chapter 2 In order to investigate the parity asymmetry, I compared the even and odd spectral parameters of WMAP data with 1000 Gaussian Mote-Carlo simulations. The results of γ, θ_c and R_* are shown below (Fig. 4.3 , 4.4, 4.5,).

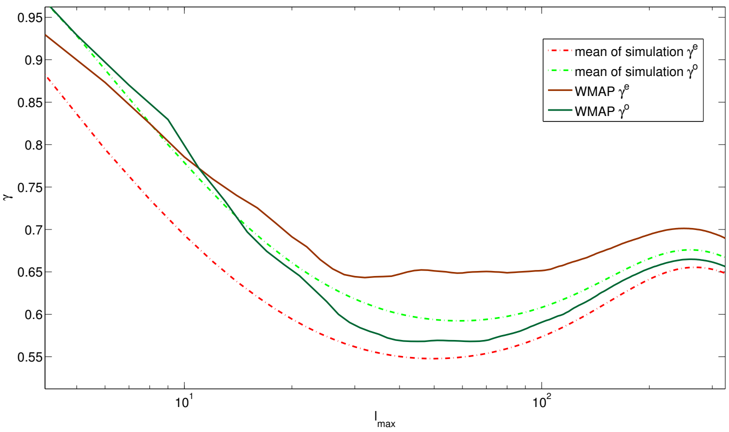

Figure 4.3: Gamma parameter - In this figure, it is clear that gamma even (dark red) of WMAP is higher than the gamma odd(dark green) of WMAP, but the mean of the simulated gamma even (light red) is lower than the mean of the simulated gamma odd (light green).

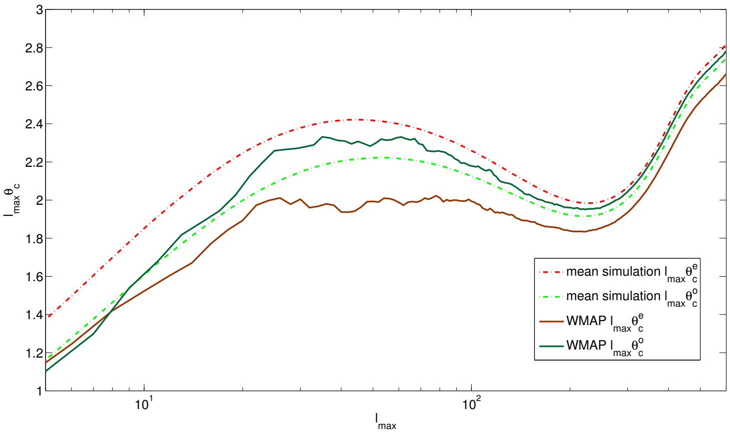

Figure 4.4: Lengthscale parameter - In this figure, lengthscale for even WMAP (dark red) is higher than the lengthscale odd(dark green) WMAP, but the mean of simulated lengthscale for even (light red) is lower than the mean of the simulated lengthscale for odd (light green).

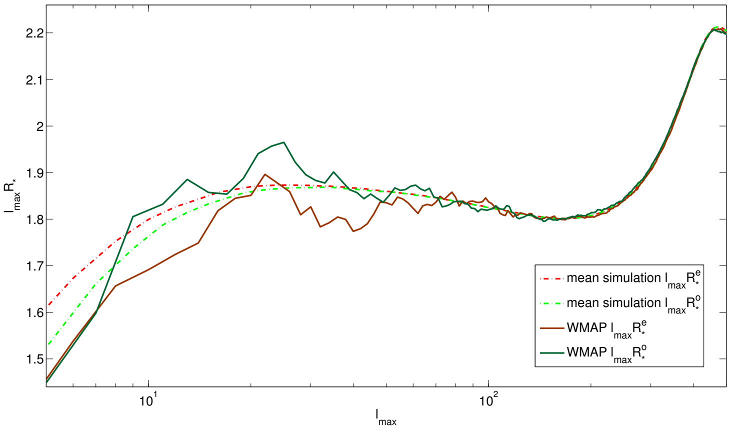

Figure 4.5: R_* - In this figure, it is clear that R_*^e (dark red) for WMAP is higher than the R_*^o(dark green) for WMAP, but the mean of the simulated R_*^e (light red) is lower than the mean of the simulated R_*^o (light green).

Note, the above figures use l_{max} as axes, because these spectral parameters not only depend on the power spectrum but are also associated with the window function, which may be effectively substitute by varying the upper limit of the l summation, because the window function falls off sharply at large l. Since a lot of white noise is located at small angular scale which corresponds to large l, and we do not know how to cut it, therefore it is better to draw the figures associated with different smooth levels, one of them could be closer to the ideal map.

Two smooth levels are considered in the following investigation, namely $l_{max} = 22$ and $l_{max} = 220$. Where $l_{max} = 22$ corresponds to the maximum of odd parity anomaly, see Fig. 2.4. The other case $l = 220$ is the location of the first peak in the power spectrum. Here, $l_{max} = 220$ is used to compare with $l_{max} = 22$, in order to distinguish the effects of the multipoles larger than 22 from the effects of the multipoles lower than 22.

	even		odd	
	$l_{max} = 22$	$l_{max} = 220$	$l_{max} = 22$	$l_{max} = 220$
γ	36	2	428	234
θ_c	87	1	261	215
R_*	275	59	55	80

Table 4.1: The number of realizations which is more extreme than WMAP 7 year data for three spectral parameters. The total number of simulation are 1000.

Gamma

Among those spectral parameters, R_* and θ_c can be consider as scale parameters. They are associated with the size of the investigated map, which could be treated as the normalization factors. Instead, γ has a strong coupling with topological and geometrical properties, especially for the cluster of peaks. From the WMAP 7 years data $\gamma^e = 0.5623$ for the smoothing $\theta_{FWHM} \sim 1°$. For the same level of smoothing, $\gamma^o = 0.5230$. According to the cluster analysis of the random Gaussian field, this difference indicates different peak clustering rate, namely that the odd parity map has a higher clustering rate. This difference of clustering rate is visible even in the ILC map, see Fig.4.6.

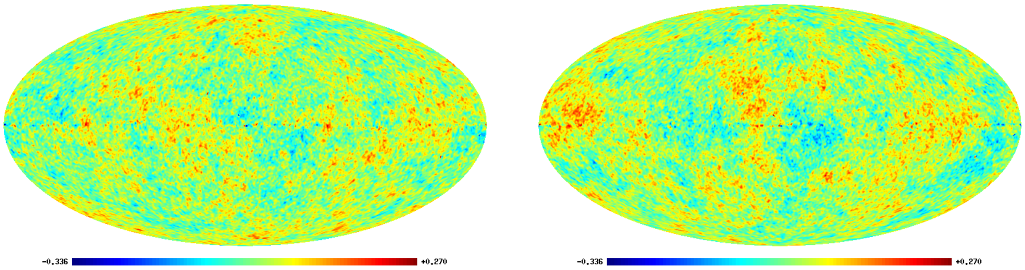

(a) Even parity map $T^+(\hat{n})$ (b) Odd parity map $T^-(\hat{n})$

Figure 4.6: Even and Odd CMB temperature map

Figure 4.3 shows the average of 1000 Gaussian Mote-Carlo simulations for γ^e and γ^o. Apparently, comparing with WMAP γ^o, WMAP γ^e further deviated from the average. Figure 4.7 provides a more compelling evidence, which describes γ^e of WMAP

7 years ILC data versus 1000 Gaussian Mote-Carlo simulations. Figure 4.9 and 4.10 demonstrate the histogram of γ^e at $l_{max} = 22$ and 220. For $l_{max} = 22$, the WMAP data is at the level of 36-in-1000. But for 220 case, only 2 realizations are larger than WMAP data. These results make me believe that this spectral parameter anomaly are not simply due to the multipoles $2 \sim 22$.

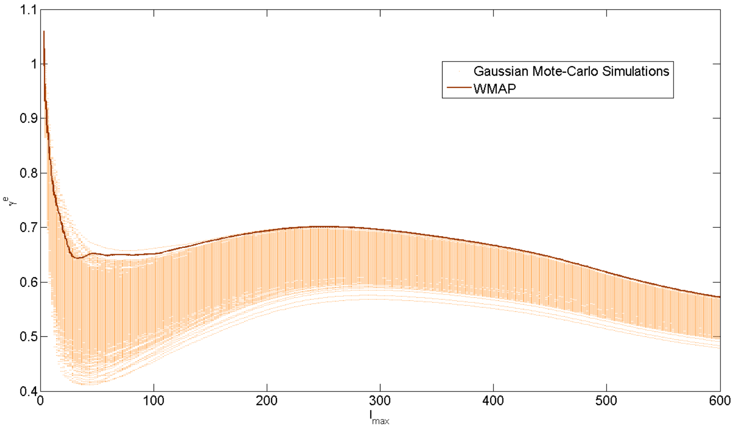

Figure 4.7: γ^e - the solid line is WMAP data, and the dots are simulations.

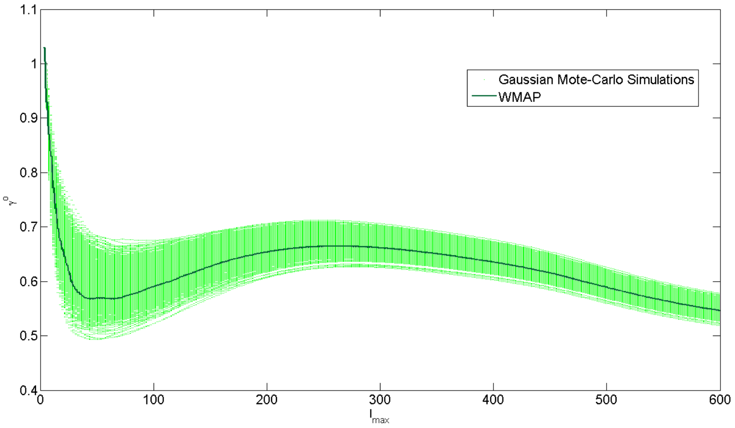

Figure 4.8: γ^o - the solid line is WMAP data, and the dots are simulations.

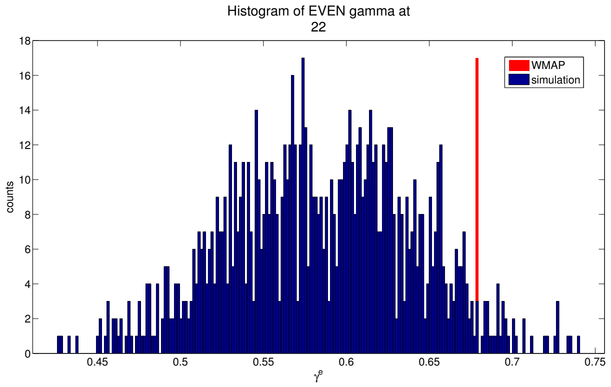

Figure 4.9: Histogram of γ^e at $l_{max} = 22$ - The red bin is WMAP data, and the blue bins are simulations.

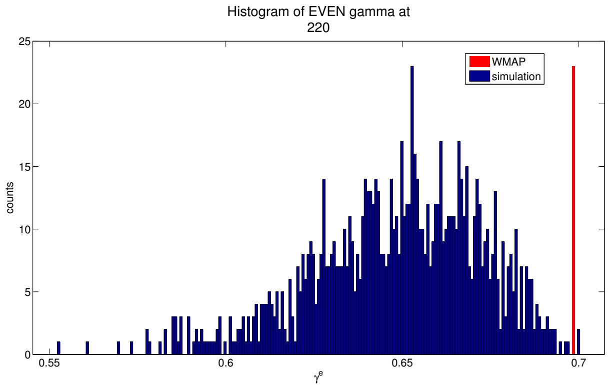

Figure 4.10: Histogram of γ^e at $l_{max} = 220$ -

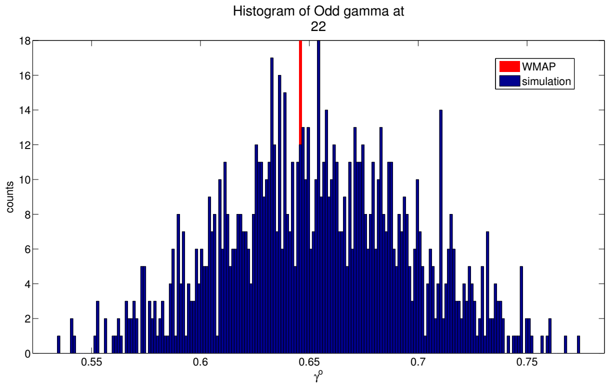

Figure 4.11: Histogram of γ^o at $l_{max} = 22$ -

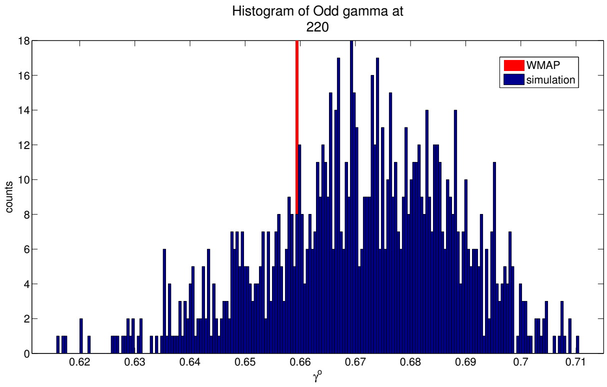

Figure 4.12: Histogram of γ^o at l_{max} = 220 - the red bin is WMAP data, and the blue bins are simulations.

Lengthscale

The same type of figures of the lengthscale θ_c are shown in Fig.4.13 to 4.15(b). The result confirmed the conclusion from γ^e figures. Not suppressed, the θ_c^e of WMAP is distinctive at the level of 1-in-1000 for $l_{max} = 220$. Accordingly this low lengthscale will directly influence the second and third Minkowski functional test, as the observed map shows longer contour length L and higher genus G than the theoretical prediction.

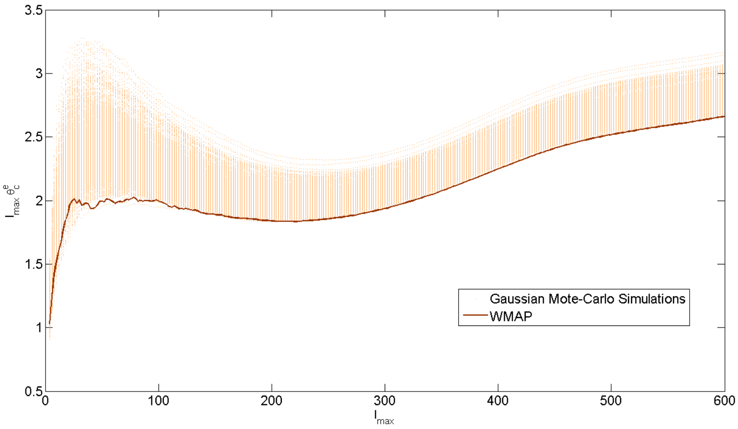

Figure 4.13: $l_{max}\theta_c^e$ - the solid line is WMAP data, and the dots are simulations.

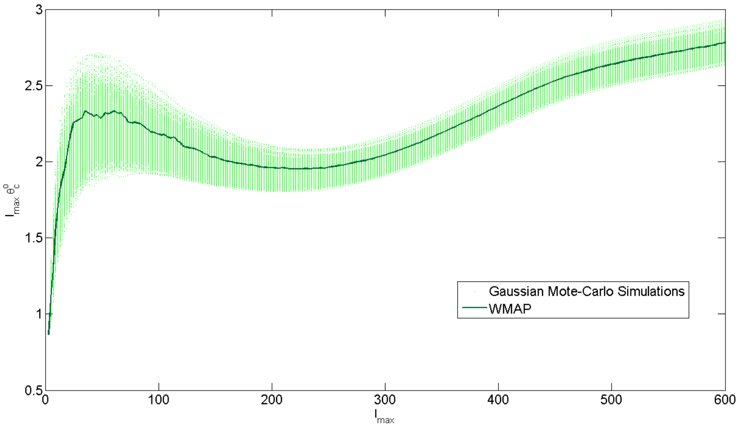

Figure 4.14: $l_{max}\theta_c^o$ - the solid line is WMAP data, and the dots are simulations.

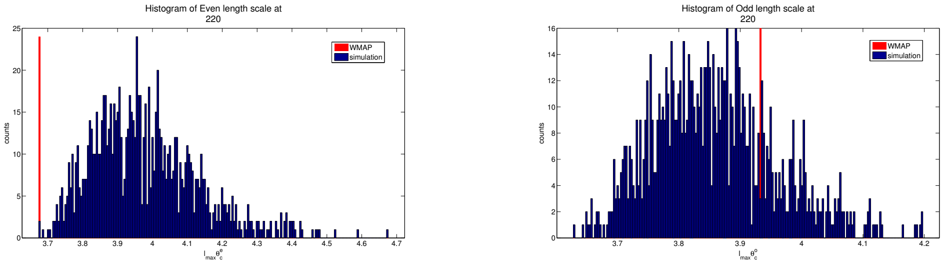

(a) Histogram of $l_{max}\theta_c^e$ at $l_{max} = 220$

(b) Hist of $l_{max}\theta_c^o$ at $l_{max} = 220$

Figure 4.15: Histogram of lengthscale even vs odd at $l_{max} = 220$

The rest figures about lengthscale are shown in Section 4.2.

R_* scale

Following D.I.Novikov and H.E.Jørgensen (1996),

$$n_{max}(-\infty, \gamma) = \frac{1}{4\pi\sqrt{3}R_*^2} \tag{4.32}$$

The total number of peaks is determined by R_*. From Fig.4.16 to 4.18(b). The R_*^e oscillates around the mean of the simulations, and the R_*^o looks anomalous. Effectively this relatively high R_*^o corresponds to less peak density. Comparing to the above two spectral parameter tests, the deviation of R_* are not as obvious as θ_c and γ.

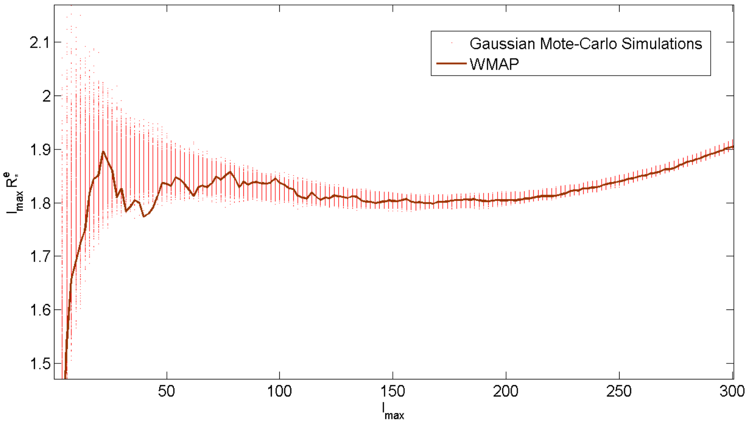

Figure 4.16: $l_{max}R^e_*$ - the solid line is WMAP data, and the dots are simulations.

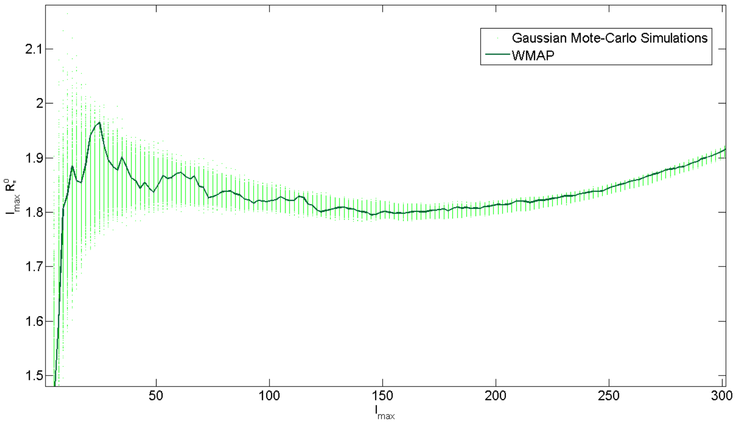

Figure 4.17: $l_{max}R^o_*$ - the solid line is WMAP data, and the dots are simulations.

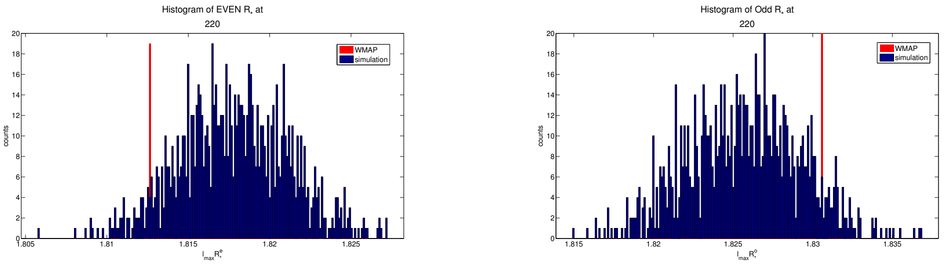

(a) Histogram of $l_{max}R^e_*$ at $l_{max} = 220$

(b) Histogram of $l_{max}R^o_*$ at $l_{max} = 220$

Figure 4.18: Histogram of R_* even vs odd at $l_{max} = 220$

Variance parameter σ_i

Further investigation is required to find out how the variance of the temperature field and its derivatives changes. The investigation of σ_0^e suggest σ_0^e of WMAP possess a roughly constant deviation from the ΛCDM model, see Fig.4.19. This constant deviation is caused by the sum of the power spectrum deviation for each even multipole. The deviations of σ_1^e and σ_2^e shows a strong correlation, and they are very likely to have the same origin. Therefore the less significant results of R are understandable. The limit of the σ_0^e's deviation in Fig.4.19 can be estimated as:

$$\Delta_0 = \frac{1}{2} \frac{\alpha}{\sigma_{0\,\Lambda CDM}^e} \tag{4.33}$$

Where α is the difference between $\sigma_{0\,\Lambda CDM}^e$ and $\sigma_{0\,WMAP}^e$ for all multipoles. Since $(\sigma_0)^2 = C(0) =< \Delta T^2 >$, we may connect the anomaly of the parity asymmetry to the variance of the temperature anisotropy. Using the One-point probability density distribution function, it is clear to see the relatively small variance in Fig.4.20.

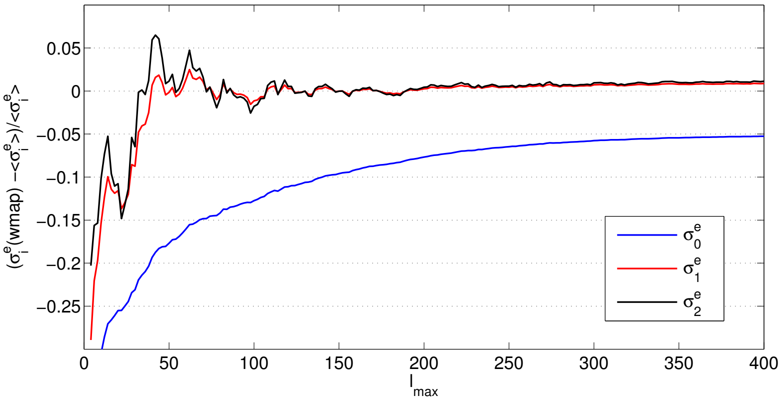

Figure 4.19: The deviation of σ_i^e - The blue line shows the deviation of σ_0^e, where it approximates a constant at large l_{max}. The red and black lines describe the deviation of σ_1^e and σ_2^e, they have almost the same oscillations. The reason for the deviation of σ_1^e and σ_2^e must be the same.

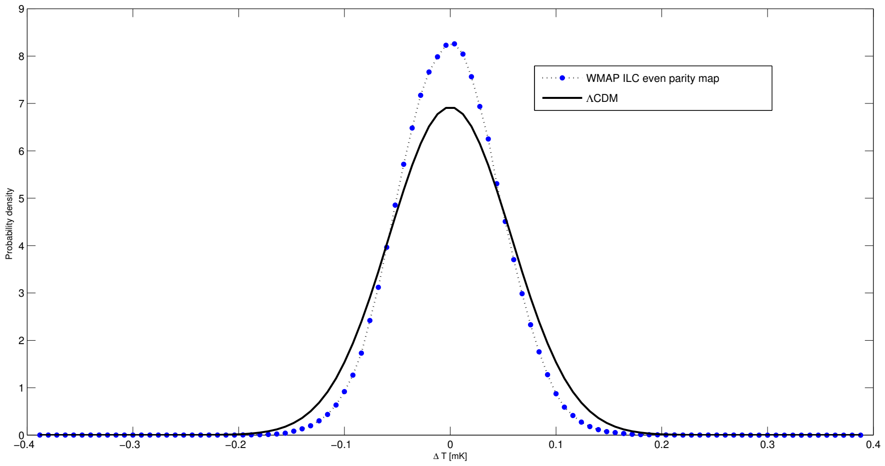

Figure 4.20: Temperature histogram of even parity map - The solid line represent the ΛCDM model, and the dash line is the one from WMAP ILC data. Obviously, the observed even parity map shows a relatively small variance compared to the prediction from the theory.

As illustrated above, the result of the γ^e test show that the observed data is significantly higher than the theoretical prediction, the probability to have such high value is remarkably low. However, the γ^o test result is in an acceptable range. θ_c^e and θ_c^o tests show the similar results. The tests indicate that the even parity temperature map is more peculiar than the odd parity map.

The comparison graphs

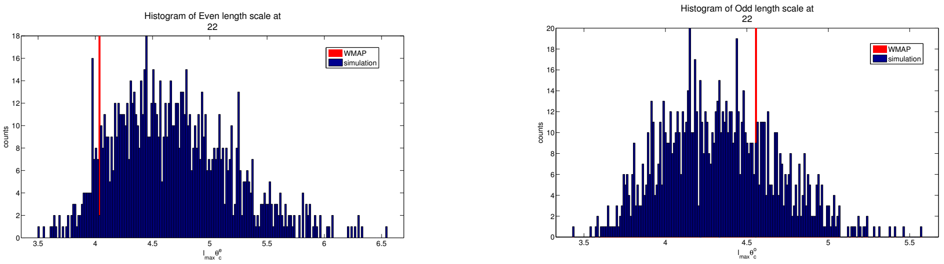

(a) Histogram of $l_{max}\theta_c^e$ at $l_{max} = 22$

(b) Histogram of $l_{max}\theta_c^o$ at $l_{max} = 22$

Figure 4.21: Histogram of lengthscale even vs odd at $l_{max} = 22$

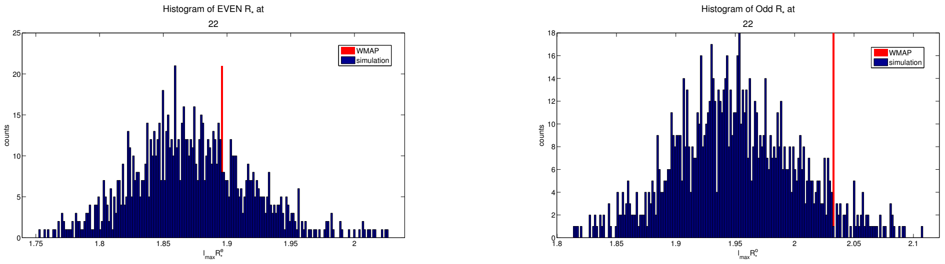

(a) Histogram of $l_{max}R^e_*$ at $l_{max} = 22$

(b) Histogram of $l_{max}R^o_*$ at $l_{max} = 22$

Figure 4.22: Histogram of R_* even vs odd at $l_{max} = 22$

Chapter 5

Primordial origin of parity asymmetry

The origin of odd parity preference may be classified into two big categories: systematic or cosmological.

The first category has been investigated by J.Kim & P.Naselsky [14]. In their work, the possible systematic origin, including asymmetric beams, instrument noise, foreground and cut-sky effect was investigated. They did not find definite association of the parity asymmetry with any known systematic effects.

On the other hand, odd parity preference may relate to a different cosmological model, such as a non-trivial topology Universe. In the following, I am going to analyse the parity symmetry of an inhomogeneous multi-connected flat universe, by starting with an introduction of some basic notions about Cosmic geometry.

5.1 The shape of universe

A Large number of astrophysical observations show that to a high degree of accuracy, our Universe is homogeneous and isotropic at scales larger than hundred megaparsecs. Isotropy states that the space looks the same in each direction. Homogeneity states that the metric of the space is the same everywhere. Our universe locally fulfills the Friedmann-Robertson-Walker model, which can be generalized as one metric and two well-known equations as below,

$$ds^2 = -dt^2 + a^2(t)[\frac{dr^2}{1-\kappa r^2} + r^2 d\Omega^2] \tag{5.1}$$

$$(\frac{\dot{a}}{a})^2 = \frac{8\pi G}{3}\rho - \frac{\kappa}{a^2} \tag{5.2}$$

$$(\frac{\ddot{a}}{a}) = -\frac{4\pi G}{3}(\rho + 3p) \tag{5.3}$$

Note κ is a curvature parameter and

$$\begin{aligned} \kappa < 0 &\iff \text{negative curvature} \\ \kappa = 0 &\iff \text{no curvature} \\ \kappa > 0 &\iff \text{positive curvature} \end{aligned}$$

Friedmann equation (Eq.5.2) can be rewritten as:

$$\Omega - 1 = \frac{\kappa}{H^2 a^2} \tag{5.4}$$

where $\Omega = \frac{8\pi G}{3H^2}\rho$ is the energy density parameter. By knowing the total energy density, we can calculate the curvature parameter κ. WMAP 7 years data indicate $\Omega = 1.0009 \pm 0.0578$. This solid evidence leads us to believe that the curvature is very close to zero, at least for the observable universe. Accordingly, there are two possible explanations, one is that the universe is flat, and the other is that the universe is curved with a curvature radius larger than the horizon radius. Since the simplest explanation is most likely to be the correct one (the Occam's razor principle), and also following the description of ΛCDM concordance model, the flat universe is then selected.

However, the flatness is not sufficient to determine our model. By considering a non-trivial topology *viz.* multi-connect space, there are 18 topological different flat space forms in three dimension [24]. Among these 18 space forms, there are eight non-orientable forms, which are not suitable for general relativity, as the signs in the Lorentzian metric will change when the vector moving around specific loops. Hence, the rest ten are of physical interest. Four of them have less than 3 compact directions, which corresponds to infinite volume and named open forms (Table 5.1). The remaining six forms, called closed forms (Table 5.2), possess 3 compact directions, and corresponds to a finite volume. They show great promise in explaining the anomalies of the CMB anisotropy at large scale.

Symbol	Name	Compact Directions	Orientable
E_{11}	chimney space	2	Yes
E_{12}	chimney space with half turn	2	Yes
E_{16}	slab space	1	Yes
E_{18}	Euclidean space	0	Yes

Table 5.1: The four locally Euclidean, open, oriented three-spaces

Symbol	Name	Fundamental polyhedron	Rotation	Rotation face
E_1	3-torus	parallelepiped	0	none
E_2	half turn space	parallelepiped	π	one pair opposite
E_3	quarter turn space	parallelepiped	$\pi/2$	one pair opposite
E_4	third turn space	parallelepiped	π	all three pairs
E_5	sixth turn space	hexagonal prism	$2\pi/3$	top to bottom
E_6	Hantzsche-Wendt space	hexagonal prism	$\pi/3$	top to bottom

Table 5.2: The six locally Euclidean, closed, oriented three-spaces. For all cases translations out of the fundamental polyhedron will come out from the opposite faces.

5.2 Closed space form

The Euclidean closed space forms are obtained as the quotient $\tilde{M}^3/\Gamma$ of Euclidean space by a discrete and fixed point free symmetry group Γ. The simplest model is E_1 in Table 5.2. It is the 3-torus which can be described as the topological product $\mathbb{S}^1 \times \mathbb{S}^1 \times \mathbb{S}^1$. This form is the only one possessing the special property of global homogeneity. In this section I will use this simple model to explain the low quadrupole and show the correlated a_{lm} in the CMB.

Normally, a D-dimensional hypersurface is much easier to imagine under $D+1$-dimensional space. But as we know, people are usually thinking in the sense of 3-dimensional space, and it will be difficult to imagine the 3-torus. Hence, the 2-torus will be used as an analogue firstly. The 2-torus $\mathbb{S}^1 \times \mathbb{S}^1$ as shown in Fig. 5.1, is obtained by connecting the opposite edges of a square. It is flat and homogeneous everywhere but globally anisotropic. In this hypersurface, if someone keeps walking along one direction, he will be back at the start point eventually. Similarly, a three dimensional torus can be obtained by connecting the opposite faces of a parallelepiped. The group Γ of 3-torus is generated by three orthogonal translations shown below.

$$\begin{aligned} \vec{x} \rightarrow \vec{x}\,' &= \vec{x} + L_x\,\vec{e}_x \\ \vec{x} \rightarrow \vec{x}\,' &= \vec{x} + L_y\,\vec{e}_y \\ \vec{x} \rightarrow \vec{x}\,' &= \vec{x} + L_z\,\vec{e}_z \end{aligned} \tag{5.5}$$

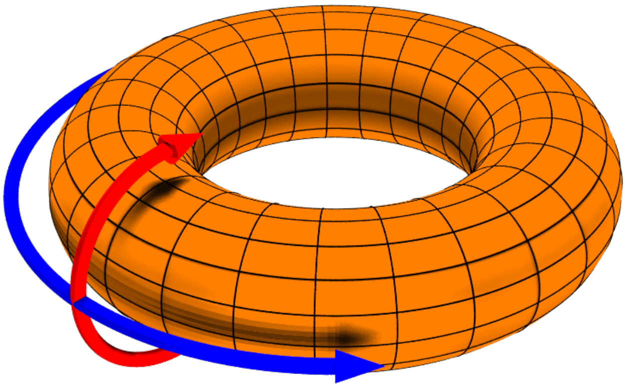

Figure 5.1: Torus - The figure show the 2 dimensional torus in 3 dimensional space. For the 3-torus, it would be much more clear to draw it in higher dimensional space similar to what we did for the 2-torus. This figure is from www.wikipedia.org

In flat geometry[1] we may write the density perturbation (scalar type) as a linear combination of plane waves:

$$\delta = \sum_{\vec{k}} \delta_{\vec{k}} e^{i\vec{k}\cdot\vec{x}} \tag{5.6}$$

In the case of a multi-connected space this perturbation must be invariant under the symmetry generators of the form of that space.

$$\delta = \sum_{\vec{k}} \delta_{\vec{k}} \exp(i\vec{k}\vec{x}) = \sum_{\vec{k}} \delta_{\vec{k}} \exp(i\vec{k}(\vec{x}+L)) \tag{5.7}$$

---

[1] Note n-torus is flat, because $\mathbb{S}^1$ is flat.

The periodic condition leads to the discrete wave vector $k_i = \frac{2\pi n}{L_i}$. As a result, this fact will finally suppress low multipoles' moment of temperature fluctuations[25]. For simplicity, according to Peebles (1982)[26], we may write the large scale temperature fluctuations as:

$$\frac{\Delta T}{T}(\theta,\phi) = -\frac{1}{2}H^2 \sum_{\vec{k}} k^{-2} \delta_{\vec{k}} \exp i\vec{k}\cdot\vec{x} \tag{5.8}$$

where $\delta_{\vec{k}}$ is the density fluctuation in Fourier space. The expansion of temperature fluctuations in spherical harmonics is

$$\begin{aligned} \frac{\delta T}{T}(\theta,\phi) &= \sum_{l,m} a_{lm} Y_{lm}(\theta,\phi) \\ a_{lm} &= -2\pi i^l H^2 \sum_{\vec{k}} k^{-2} \delta_{\vec{k}} j_l(k\eta_0) Y_{lm}(\Omega_{\vec{k}}) \end{aligned} \tag{5.9}$$

where $j_l(k\eta_0)$ is the lth-order spherical Bessel function, and η_0 is the present conformal time. Since some k are not allowed, the integration

$$\int_{\Omega_{\vec{k}}} Y_{lm}(\hat{k}) Y^*_{l'm'}(\hat{k})\, dk = \delta_{ll'}\delta_{mm'} \tag{5.10}$$

will not exist. Hence we are need to consider the non-diagonal terms in the covariance matrix $\langle a_{lm} a_{l'm'} \rangle$. From another point of view, the non-trivial topology breaks the random properties of the primordial inhomogeneity, since the correlations are added. As a result, we cannot estimate C_l as before, instead we define

$$C_l := \frac{1}{2l+1} \sum_{m=-l}^{l} < |a_{lm}|^2 > \tag{5.11}$$

Substituting Eq.5.9 in,

$$C_l = \frac{1}{2l+1} 4\pi^2 H^4 \sum_{\vec{k}} k^{-4} |\delta_{\vec{k}}|^2 j_l(k\eta_0)^2 \tag{5.12}$$

In order to simplify the analysis, we assume $|\delta_{\vec{k}}|^2 \propto k^n$ and consider the cubic 3-torus case, i.e. $L_x = L_y = L_z = L$. So the length of k is:

$$|k| = \frac{2\pi}{L}\sqrt{n_x^2 + n_y^2 + n_z^2} \qquad n_x, n_y, n_z \in \mathbb{Z} \tag{5.13}$$

When n_x, n_y, n_z are small, the interval between two neighboring k is wide. On the contrary, as n_x, n_y, n_z approaches infinity, $|k|$ will approximate to continuous. Accordingly the absence of some k modes will suppress low multipoles in the power spectrum of the CMB anisotropy C_l [25] . However, this is only significant at large scales (especially for the quadrapole), because the right hand of Eq.5.12 exhibits a main peak at $k\eta_0 \sim l$, see Figure 5.2(a),5.2(b) and 5.2(c). For small angular scales, i.e. big l, the main peak is located at a large k. The contribution of the vector k 'quantization' can be neglected, since when k is large, the interval between allowed k is relative small.

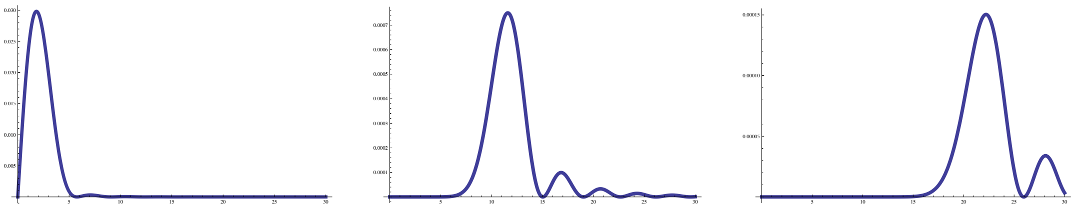

(a) $l = 2$ (b) $l = 10$ (c) $l = 20$

Figure 5.2: lth-order spherical Bessel function

Alternatively, the same result can be obtained from trivial topology model by adding constraints on wave vectors. Suppose there is a limitation of small k in the primordial density perturbation. This constraint will result in the suppression in low multipoles. Since the CMB temperature field is the sum of even and odd parity temperature fields as seen in Eq.2.5, if the constraints are only applied to the even parity temperature field $T^+(\hat{n})$, then the reason for odd-parity preference will be revealed.

5.3 Half-turn space

In this section I am going to explain parity asymmetry at low multipoles by breaking spatial homogeneity. It is worth to note that the 3-torus is the only one possessing homogeneity of the models in Table 5.2. In fact global homogeneity is not necessary for our universe in the sense that it could be homogeneous inside the fundamental polyhedron, and inhomogeneous beyond that scale. The simplest model without homogeneity, but with finite volume and orientations, is the half-turn space E_2.

Following R.Aurich and S.Lustig[27], the half-turn space could be generated by the three transformations

$$\vec{x} \to \vec{x}\,' = \vec{x} + L_x \, \vec{e}_x$$

$$\begin{aligned} \vec{x} \to \vec{x}\,' &= \vec{x} + L_y\,\vec{e}_y \\ \vec{x} \to \vec{x}\,' &= \vec{x}_{\mathrm{R}} + L_z\,\vec{e}_z \end{aligned} \tag{5.14}$$

where $\vec{x}_{\mathrm{R}} = (-x\,L_x, -y\,L_y, z\,L_z)$ takes the 180°-rotation of $\vec{x}$ in the xy-plane. [1] Here equal-length scales $L_x = L_y = L_z = L$ are selected for convenience. The half-turn space is illustrated in Fig.5.3 where the special z-transformation leads to an inhomogeneous space form.

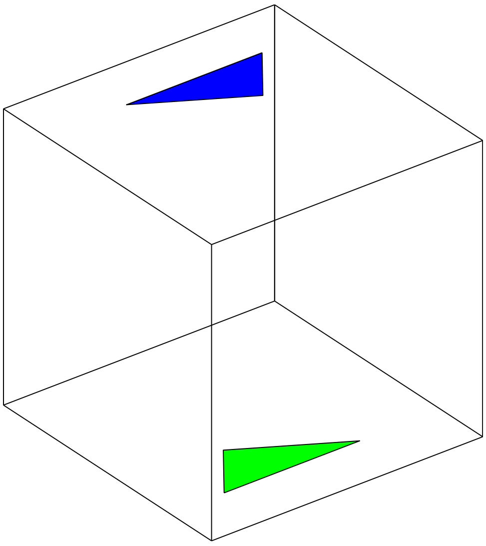

Figure 5.3: Half-Turn space - The sketch illustrates the fundamental polyhedron of equal length scale half-turn space. Reprint from R.Aurich and S.Lustig [27]

Since the perturbation must be invariant under the action of the generators of the symmetry group Γ, the eigenfunction of half-turn space can be derived by requiring equation

$$\Psi_{\vec{k}}\,(\vec{x}\,) = \exp\left(\mathrm{i}\,\vec{k}\cdot\vec{x}\right) \tag{5.15}$$

to be invariant under the transformations:

$$\Psi_{\vec{k}}\,(x, y, z) = \Psi_{\vec{k}}\,(x\vec{e}_x + y\vec{e}_y + z\vec{e}_z\, + n_x \cdot L_x\vec{e}_x\,)$$

---

[1] It is not necessary to take this rotation in the xy-plane, you are free to choose a plane among xy,yz,xz.

$$\begin{aligned}\Psi_{\vec{k}}\,(x,y,z) &= \Psi_{\vec{k}}\,(x\vec{e}_x + y\vec{e}_y + z\vec{e}_z\ + n_y\cdot L_y\vec{e}_y\,) \\ \Psi_{\vec{k}}\,(x,y,z) &= \Psi_{\vec{k}}\,(-x\vec{e}_x - y\vec{e}_y + z\vec{e}_z\ + n_z\cdot L_z\vec{e}_z) \end{aligned} \tag{5.16}$$

Note, the last line uses the Eq.5.14 of z axis. These imply a new constraint for k_z,

$$\exp(i2\,k_z\,L_z) = 1 \tag{5.17}$$

The x and y axis transformation is the same as the Γ transformations of the 3-torus, the z axis transformation, $\vec{k} = 2\pi(n_x/L, n_y/L, n_z/2L)$ transforms into $\vec{k}' = 2\pi(-n_x/L, -n_y/L, n_z/2L)$.
For $n_x, n_y = 0$ and $n_z \in$ even number

$$\Psi_{\vec{k}}\,(\vec{x}\,) \;=\; \exp\left(\mathrm{i}\,\vec{k}\cdot\vec{x}\right) \tag{5.18}$$

and for $n_x \in \mathbb{N}$, n_y, $n_z \in \mathbb{Z}$ or $n_x = 0$, $n_y \in \mathbb{N}$, $n_z \in \mathbb{Z}$ by

$$\Psi_{\vec{k}}\,(\vec{x}\,) \;=\; \frac{1}{\sqrt{2}}\left[\exp\left(\mathrm{i}\,\vec{k}\cdot\vec{x}\right) + (-1)^{n_z}\exp\left(\mathrm{i}\,\vec{k}'\cdot\vec{x}\right)\right] \quad . \tag{5.19}$$

We may rewrite the eigenfunction of the Laplacian in the inhomogeneous space as

$$\Psi_{\vec{k}}\,(\vec{x},\vec{x}_o) \;=\; \exp\left(\mathrm{i}\,\vec{k}\cdot(\vec{x}-\vec{x}_0)\right)\cdot\exp\left(\mathrm{i}\,\vec{k}\cdot(\vec{x}_0)\right) \tag{5.20}$$

The computation of the CMB anisotropy requires the expansion of the eigenfunctions with respect to the spherical basis.

$$\Psi_{\vec{k}}\,(r,\hat{n},\vec{x}_o) \;=\; \sum_{l,m}\xi^{\vec{k}}_{lm}(\vec{x}_o)R_{k\,l}(r)\,Y_{l\,m}(\hat{n}) \tag{5.21}$$

where $R_{k\,l}(r) = 4\pi\,j_l(kr)$ is the radial function, i. e. the spherical Bessel function, $Y_{l\,m}(\hat{n})$ the spherical harmonics. Here r and $\hat{n}$ is with respect to the position of the observer $\vec{x}_o$, as

$$\begin{aligned} r &= |\vec{x}-\vec{x}_o| \\ \hat{n} &= \frac{(\vec{x}-\vec{x}_o)}{r} \end{aligned} \tag{5.22}$$

Note,

$$e^{i\vec{k}\cdot\vec{n}} = 4\pi\sum_{l,m} i^l j_l(kr)Y_{lm}(\hat{n})Y^*_{lm}(\hat{k}) \tag{5.23}$$

In fact i^l and $Y^*_{lm}(\hat{k})$ are contained in the coefficient $\xi^{\vec{k}}_{lm}(\vec{x}_o)$. The expansion coefficients $\xi^{\vec{k}}_{lm}(\vec{x}_o)$ for Eq.5.18 are given by

$$\xi^{\vec{k}}_{lm}\,(\vec{x}_o) \;=\; \mathrm{i}^l\, Y^*_{lm}(\hat{k})\, \exp\left(\mathrm{i}\,\vec{k}\cdot\vec{x}_o\right) \tag{5.24}$$

and for Eq.5.19

$$\begin{aligned}\xi^{\vec{k}}_{lm}\,(\vec{x}_o) &= \frac{\mathrm{i}^l}{\sqrt{2}}\left[Y^*_{lm}(\hat{k})\,\exp\left(\mathrm{i}\,\vec{k}\cdot\vec{x}_o\right) + (-1)^{n_z}\,Y^*_{lm}(\hat{k}\,')\,\exp\left(\mathrm{i}\,\vec{k}\,'\cdot\vec{x}_o\right)\right]\\ &= \frac{\mathrm{i}^l}{\sqrt{2}}\,Y^*_{lm}(\hat{k})\,\left[\exp\left(\mathrm{i}\,\vec{k}\cdot\vec{x}_o\right) + (-1)^{n_z+m}\,\exp\left(\mathrm{i}\,\vec{k}\,'\cdot\vec{x}_o\right)\right]\end{aligned} \tag{5.25}$$

where $Y^*_{lm}(\hat{k}\,') = (-1)^m Y^*_{lm}(\hat{k})$, $\hat{k} = \vec{k}/k$, and $\hat{k}\,' = \vec{k}\,'/k$. The temperature fluctuations of the CMB can be expressed as linear combination of the spherical harmonics, and the weighting coefficients a_{lm} for the half-turn space are determined by

$$a_{lm} \;=\; \sum_{\vec{k}} T_l(k)\;\Phi_{\vec{k}}\;\xi^{\vec{k}}_{lm}(\vec{x}_o) \tag{5.26}$$

where the sum runs over the allowed values of $\vec{k}$. Compared with the 3-torus, the half-turn space, as discussed above, have more k modes since $2k_zL = 2\pi N \quad N \in \mathbb{Z}$. $T_l(k)$ is the radiation transfer function containing the Sachs-Wolfe effect, the Doppler contribution, the Integrated Sachs-Wolfe effect and etc.

In the case of first kind coefficient $\xi^{\vec{k}(\vec{x}_o)}_{lm}$,

$$a_{lm} \;=\; \mathrm{i}^l \sum_{\vec{k}}^{\text{half}} T_l(k)\;\,Y^*_{lm}(\hat{k})\,[f(\vec{k}) \,+ (-1)^l\, f^*(\vec{k})] \tag{5.27}$$

$$f(\vec{k}) \equiv \Phi_{\vec{k}}\;\exp\left(\mathrm{i}\,\vec{k}\cdot\vec{x}_o\right) \tag{5.28}$$

Here we used the reality condition of $\Phi_{\vec{x}}$ ($\Phi_{-\vec{k}} = \Phi^*_{\vec{k}}$), and half means sum over the hemisphere of all the allowed k vectors.
when l is even.

$$a_{lm} \;=\; \frac{\mathrm{i}^l}{2} \sum_{\vec{k}}^{\text{half}} T_l(k)\;\,Y^*_{lm}(\hat{k})\,Re[f(\vec{k})] \tag{5.29}$$

when l is odd.

$$a_{lm} = \frac{\mathrm{i}^l}{2} \sum_{\vec{k}}^{\text{half}} T_l(k)\ Y^*_{lm}(\hat{k})\, Im[f(\vec{k})] \tag{5.30}$$

We may see that the odd-parity preference might be produced.

$$|Im[f(\vec{k})]| \gg |Re[f(\vec{k})]| \quad \text{for } l < 22 \tag{5.31}$$

$$Im[f(\vec{k})] = Re[\Phi_{\vec{k}}]\ \sin\theta\ + Im[\Phi_{\vec{k}}]\ \cos\theta \tag{5.32}$$

$$Re[f(\vec{k})] = Re[\Phi_{\vec{k}}]\ \cos\theta\ - Im[\Phi_{\vec{k}}]\ \sin\theta \tag{5.33}$$

where $\theta = \vec{k} \cdot \vec{x}_o$. For simplicity, R and I will be used for the real and imaginary part of the primordial perturbation $\Phi_{\vec{k}}$ hereafter.

$$\Phi_{\vec{k}} = \ R\ +\ \mathrm{i}\, I \tag{5.34}$$

Due to the special property of the radiation transfer function, the temperature anisotropy will approximate to zero unless $l \sim k\eta_0$. As a result

$$|Im[f(\vec{k})]| \gg |Re[f(\vec{k})]| \quad \text{for } k\ <\ 22/\eta_0 \tag{5.35}$$

$$|R\ \sin\theta\ + I\ \cos\theta| \gg |R\ \cos\theta\ - I\ \sin\theta| \tag{5.36}$$

Here we assume $|R| \approx |I|$. Hence,

$$(1)\ \ \text{If}\ \ \ RI\ >\ 0\ \ \text{then}\ \ |\sin\theta\ +\ \cos\theta| \gg |\ \cos\theta\ -\ \sin\theta| \tag{5.37}$$

$0 < \theta < \pi/2$ corresponds to the odd-parity preference. $-\pi/2 < \theta < 0$ corresponds to the even-parity preference. Both of them have a period π.

$$(2)\ \ \text{If}\ \ \ RI\ <\ 0\ \ \text{then}\ \ |\ \cos\theta\ -\ \sin\theta| \gg |\sin\theta\ +\ \cos\theta| \tag{5.38}$$

$-\pi/2 < \theta < 0$ corresponds to the odd-parity preference. $0 < \theta < \pi/2$ corresponds to the even-parity preference. See figure 5.4.

$$(3)\ \ \ \text{If}\ \ \ I\ =\ 0\ \ \text{then}\ \ |\sin\theta| \gg |\cos\theta| \tag{5.39}$$

$\pi/4 < \theta < 3\pi/4$ corresponds to the odd-parity preference. $-\pi/4 < \theta < \pi/4$ corresponds to the even-parity preference.

$$(4)\ \ \ \text{If}\ \ \ R\ =\ 0\ \ \text{then}\ \ |\cos\theta| \gg |\sin\theta| \tag{5.40}$$

$-\pi/4 < \theta < \pi/4$ corresponds to the odd-parity preference. $\pi/4 < \theta < 3\pi/4$ corresponds to the even-parity preference. both of them have a period π.

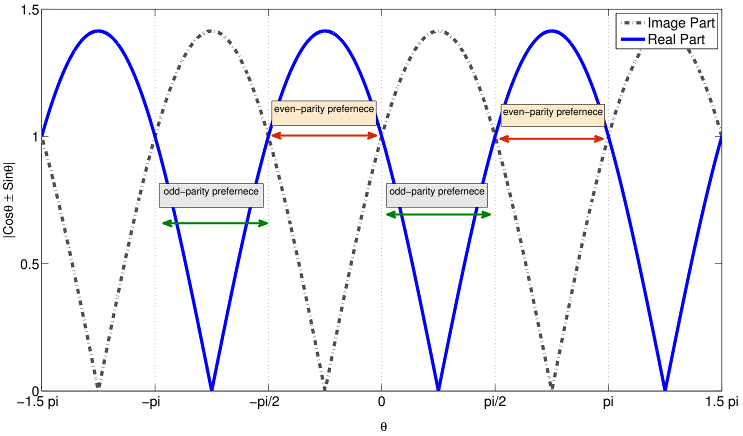

Figure 5.4: Figure of periodic parity preference - The plot illustrates the imaginary part and real part of $f(\vec{k})$ defined in equation 5.28. (This plot is under $RI > 0$ condition. For $RI < 0$ case interchange even and odd parity regions)

It is easy to find that θ depends on 2 parameters: one is k which relates to l, and the other one is x_0. Obviously x_0 should be fixed. So it means that when we vary l , the parity preference would alter. Therefore, we should see some even parity preferences as well. In C.L.Bennett (2011) [28] they found even parity preference at $l = 300 \sim 349$. There is another possible solution. If the region is sufficiently large, say, $2 < l < 700$ or even wider, the parity preference will not change on the current observable angular scale.

The investigations above are based on the first kind coefficient $\xi_{lm}^{\vec{k}(\vec{x}_o)}$ of half-turn space, this eigenfunction is mathematically equivalent to a inhomogeneous torus. Now, recall the a_{lm} of the second kind coefficient $\xi_{lm}^{\vec{k}(\vec{x}_o)}$,

$$a_{lm} = \sum_{\vec{k}} T_l(k)\, \frac{\mathrm{i}^l}{\sqrt{2}}\, Y_{lm}^{*}(\hat{k})\, \Phi_{\vec{k}}\, \left[\exp\left(\mathrm{i}\,\vec{k}\cdot\vec{x}_o\right) + (-1)^{n_z+m}\, \exp\left(\mathrm{i}\,\vec{k}\,'\cdot\vec{x}_o\right)\right]$$

If $n_z + m = even$,

$$a_{lm} = \frac{\mathrm{i}^l}{\sqrt{2}} \sum_{\vec{k}} T_l(k)\, cosB\, Y_{lm}^{*}(\hat{k})\, [f(\vec{k}) + (-1)^l\, f^{*}(\vec{k})] \qquad (5.41)$$

If $n_z + m = odd$

$$a_{lm} \ = \frac{\mathrm{i}^{l+1}}{\sqrt{2}} \sum_{\vec{k}} T_l(k) \ sinB \ Y^*_{lm}(\hat{k}) \, [f(\vec{k}) + (-1)^l \, f^*(\vec{k})] \tag{5.42}$$

$$f(\vec{k}) := \Phi_{\vec{k}} \ \exp{(\mathrm{i} \ A)} \tag{5.43}$$

where $A = k_z \cdot x_z$, and $B = k_x x_x + k_y x_y$. By repeating the procedures that we did with the first eigenfunction, the same expressions can be found except that θ will be replaced by A in Eq.5.37 Eq.5.38 Eq.5.39 Eq.5.40.

The above discussion have shown that the non-trivial topology model could be a source of parity asymmetry. By introducing a inhomogeneity coefficient $\xi^{\vec{k}(\vec{x}_o)}_{lm}$, I have shown the parity preference for difference angular scales depends on the observer's position. Our universe could be placed at one of those odd preference regions.

Chapter 6

Discussion and conclusion

By using the released WMAP 7 years data, the morphological properties of the even parity map and odd parity map has been investigated separately. The WMAP data of the γ^e and θ_c^e show contradictory results that the observed γ^e and θ_c^e are significant larger (lower for θ_c^e) than theoretical simulations. On the other hand, the γ^o and θ_c^o tests show no significant difference. (see Table 4.1) This implies that the even parity map $T^+(\hat{n})$ may contain some unexpected anomaly, in the sense that the even power spectrum is suppressing, or in other words odd parity preference.

Based on the results of Chapter 4, some features of the theoretical expected map can be obtained from the ΛCDM models by using the morphology analysis. Compared with the observation, the theoretical expected even parity map possesses relatively higher cluster rate, shorter contour length and less genus. Hence, it is 'smoother' than the observed even parity map. This may indicate some non-Gaussianity contaminations.

Chapter 5 investigated possible primordial cosmological origins. It has been shown that the non-trivial topological models could generate an odd parity preference map, if the universe is inhomogeneous and an appropriate observer position is chosen.

Due to lack of further evidence, the origin of the odd parity preference anomaly still remains unclear. Recent investigations suggests that the odd parity preference anomaly may not be isolated, Kim and Naselsky[29] showed that the odd parity preference at low multipoles is, in fact, the phenomenological origin of the anomaly at large-angle correlation. Whatever the origin is, the further unification of the anomalies, associated with odd parity preference, will provide us with more clues about their origin.

References

[1] A. Penzias and R. Wilson. A measurement of excess antenna temperature at 4080 mc/s. *Apj*, 142:419–421, July 1965. 1

[2] J. C. Mather, D. J. Fixsen, R. A. Shafer, C. Mosier, and D. T. Wilkinson. Calibrator design for the cobe far-infrared absolute spectrophotometer (firas). *ApJ*, 512:511–520, February 1999. 1

[3] *Cosmological Inflation and Large-Scale Structure.* Cambridge University Press, 2000. 1

[4] L. Raul Abramo and Thiago S. Pereira. Testing gaussianity, homogeneity, and isotropy with the cosmic microwave background. *Advances in Astronomy*, 2010. 2

[5] Chen Ning Yang. The law of parity conservation and other symmetry laws of physics. *Nobel Lecture*, 1957. 2

[6] T. D. Lee and C. N. Yang. Question of parity conservation in weak interactions. *Phys. Rev.*, 104(1):254–258, Oct 1956. 3

[7] Arthur Lue, Limin Wang, and Marc Kamionkowski. Cosmological signature of new parity-violating interactions. *Phys. Rev. Lett.*, 83(8):1506–1509, Aug 1999. 3

[8] K.Land and J.Magueijo. Is the universe odd. *Phys.Rev.D*, 72(10):101302, 2005. 3

[9] Jaiseung Kim and Pavel Naselsky. Anomalous parity asymmetry of the wilkinson microwave anisotropy probe power spectrum data at low multipoles. *The Astrophysical Journal Letters*, 714(2):L265, 2010. 3

[10] J.C.Mather, . M.G.Hauser, C.L.Bennett, N.W.Boggess, E.S.Cheng, Jr.Eplee, H.T.Freudenreich, R.B.Isaacman, T.Kelsall, and S.Gulkis. Early results from the cosmic background explorer (cobe). *Advances in Space Research*, 11:181–191, 1991. 3

[11] D. N. Spergel, L. Verde, H. V. Peiris, E. Komatsu, M. R. Nolta, C. L. Bennett, M. Halpern, G. Hinshaw, N.Jarosik, A. Kogut, M. Limon, S. S. Meyer, L. Page, G. S. Tucker, J. L. Weiland, E. Wollack, and E. L. Wright. First-year wilkinson microwave anisotropy probe (wmap) observations: Determination of cosmological parameters. *The Astrophysical Journal Supplement Series*, 148(1):175, 2003. 3

[12] ESA. *Bluebook Planck.* 2005. 3

[13] M. White and M. Srednicki. Window functions of cosmic microwave background experiments. *Apj*, 443:6–10, April 1995. 5

[14] Jaiseung Kim and Pavel Naselsky. Anomalous parity asymmetry of wmap 7-year power spectrum data at low multipoles: Is it cosmological or systematics? *Phys. Rev. D*, 82(6):063002, Sep 2010. 6, 8, 9, 38

[15] A. Gruppuso, F. Finelli, P. Natoli, F. Paci, P. Cabella, A. De Rosa, and N. Mandolesi. New constraints on parity symmetry from a re-analysis of the wmap-7 low-resolution power spectra. *Monthly Notices of the Royal Astronomical Society*, 411(3):1445–1452, 2011. 9

[16] Jaiseung Kim and Pavel Naselsky. Parametric tension between even and odd multipole data of the wmap power spectrum: Unaccounted contamination or missing parameters? *The Astrophysical Journal Letters*, 724(2):L217, 2010. 9

[17] K.R. Mecke, T. Buchert, and H. Wagner. Robust morphological measures for large-scale structure in the universe. *Astron. Astrophys*, 288:697–704, August 1994. 13

[18] D. Novikov, H. A. Feldman, and S. F. Shandarin. Minkowski functionals and cluster analysis for cmb maps. *International Journal of Modern Physics D*, 8:291–306, 1999. 13

[19] H. Hadwiger. Ungelste probleme nr. 20. *Elemente der Mathematik*, 1957. 13

[20] D. I. Novikov and H. E. Jørgensen. A theoretical investigation of the topology of the cosmic microwave background anisotropy on the scale 1. *The Astrophysical Journal*, 471(2):521, 1996. 16

[21] J. M. Bardeen, J. R. Bond, N. Kaiser, and A. S. Szalay. The statistics of peaks of gaussian random fields. *Apj*, 304:15–61, May 1986. 21

[22] *The Geometry of Random Fields.* 1981. 22

[23] J. R. Bond and G. Efstathiou. The statistics of cosmic background radiation fluctuations. *Royal Astronomical Society*, 226:655–687, June 1987. 23, 25

[24] Cosmic topology. *Physics Reports*, 254(3):135 – 214, 1995. 39

[25] Daniel Stevens, Douglas Scott, and Joseph Silk. Microwave background anisotropy in a toroidal universe. *Phys. Rev. Lett.*, 71(1):20–23, Jul 1993. 42, 43

[26] P. J. E. Peebles. Large-scale background temperature and mass fluctuations due to scale-invariant primeval perturbations. *Apjl*, 263:L1–L5, December 1982. 42

[27] R.Aurich and S.Lustig. Cosmic microwave anisotropies in an inhomogeneous compact flat universe. 2010. 43, 44

[28] C. L. Bennett, R. S. Hill, G. Hinshaw, D. Larson, K. M. Smith, J. Dunkley, B. Gold, M. Halpern, N. Jarosik, A. Kogut, E. Komatsu, M. Limon, S. S. Meyer, M. R. Nolta, N. Odegard, L. Page, D. N. Spergel, G. S. Tucker, J. L. Weiland, E. Wollack, and E. L. Wright. Seven-year wilkinson microwave anisotropy probe (wmap) observations: Are there cosmic microwave background anomalies? *The Astrophysical Journal Supplement Series*, 192(2):17, 2011. 48

[29] Jaiseung Kim and Pavel Naselsky. Lack of angular correlation and odd-parity preference in cmb data. *ApJ*, 2011. 50